The impacts of Stratospheric Aerosol Injection on Antarctic ice loss depend on injection location

P. B. Goddard[1], B. Kravitz[1,2], D. G. MacMartin[3], D. Visioni[3], E. M. Bednarz[3,4,5], and W. R. Lee[3]

[1]Indiana University, Bloomington, IN, USA.

[2]Pacific Northwest National Laboratory, Richland, WS, USA.

[3]Cornell University, Ithaca, NY, USA.

[4]CIRES, University of Colorado, Boulder, CO, USA.

[5]NOAA Chemical Sciences Laboratory, Boulder, CO, USA.

Corresponding author: Paul B. Goddard (pgoddard@iu.edu)

Key Points:

- Antarctic atmospheric circulation responds differently to stratospheric aerosol injections that vary by amount and injection latitude(s)
- Changes to the coastal winds impacts surface ice accumulation and shelf ocean temperatures near ice shelves
- Specific injection strategies can slow 21st century ice loss and avoid identified thresholds pertaining to Antarctic tipping points

Abstract

Owing to increasing greenhouse gas emissions, the West Antarctic Ice Sheet as well as a few subglacial basins in East Antarctica are vulnerable to rapid ice loss in the upcoming decades and centuries, respectively. This study examines the effectiveness of using Stratospheric Aerosol Injection (SAI) that minimizes global mean temperature (GMT) change to slow projected 21st century Antarctic ice loss. We use eleven different SAI cases which vary by the latitudinal location(s) and the amount(s) of the injection(s) to examine the climatic response near Antarctica in each case as compared to the reference climate at the turn of the last century. We demonstrate that injecting at a single latitude in the northern hemisphere or at the Equator increases Antarctic shelf ocean temperatures pertinent to ice shelf basal melt, while injecting only in the southern hemisphere minimizes this temperature change. We use these results to analyze the results of more complex multi-latitude injection strategies that maintain GMT at or below 1.5°C above the pre-industrial. All these cases will slow Antarctic ice loss relative to the mid-to-late 21st century SSP2-4.5 emissions pathway. Yet, to avoid a GMT threshold estimated by previous studies pertaining to rapid West Antarctic ice loss (~1.5°C above the pre-industrial), our study suggests SAI would need to cool below this threshold and predominately inject at low southern hemisphere latitudes. These results highlight the complexity of factors impacting the Antarctic response to SAI and the critical role of the injection strategy in preventing future ice loss.

Plain Language Summary

Large portions of the Antarctic ice sheet are imminently vulnerable to melting as global temperatures rise over the 21st century. This melt would lead to consequential sea level rise intensifying coastal flooding and causing large economic and ecological costs. One idea to slow global warming and limit such climate risks, is to deliberately cool the planet by placing reflective particles in the atmosphere to deflect sunlight before it warms the Earth's surface. This idea is called Stratospheric Aerosol Injection (SAI). Here, our computer simulations show that Antarctic ice loss can be slowed by using SAI, however, the results depend on the location of the aerosol injection (Equator, tropics, or high latitude). We show that putting the particles between 30°N and 30°S with the majority placed in the southern hemisphere has the best potential to slow 21st century Antarctic ice loss in our computer simulations. This study is an example of how various SAI strategies (such as, where to put these particles) can lead to very different regional climate impacts – a result that decision makers must thoroughly consider.

1 Introduction

Global climate models are an important tool for the geoengineering research community that allow the analysis of a variety of stratospheric aerosol injection (SAI) cases (how much aerosol to inject, at which latitude(s), and during which season(s)) (e.g., Tilmes et al., 2017; Dai et al., 2018; Visioni et al., 2020; MacMartin et al., 2022). These SAI cases are designed to potentially ameliorate some of the negative consequences of climate change, such as global mean temperature rise, shifts in precipitation patterns and amount, and Arctic sea ice loss (e.g., Tilmes et al., 2013; Berdahl et al., 2014; Moore et al., 2014; Kravitz et al., 2016; Lee et al., 2023). However, the impact of various SAI cases on the Antarctic region has so far not been extensively studied (McCusker et al., 2015).

The Antarctic ice sheet is currently losing mass as its marine-terminating glaciers increase in velocity and more rapidly transport ice into the Southern Ocean without a compensating increase in snowfall accumulation in its interior (Rignot et al., 2019). Propelling the outlet glaciers towards the ocean is the consequence of the reduced buttressing of the ice shelves due to enhanced basal melt and calving (Alley et al., 2015; Jenkins et al., 2016). Furthermore, warming above the ice shelves can increase surface meltwater and contribute to the deepening of crevasses that lead to iceberg calving and the potential of ice-cliff instability (e.g., Scambos et al., 2004; DeConto and Pollard, 2016; Bassis et al., 2021). Ice shelf basal melt rates increase when relatively warm Circumpolar Deep Water (CDW, about 2°C - 4°C above the seawater freezing point (Whitworth et al., 1998)) is transported from the ocean interior onto the continental shelf towards the ice sheet grounding lines, effectively melting the ice shelves from below and potentially leading to ice-shelf instability (Weertman, 1974; Rignot and Jacobs, 2002; Schoof, 2007; Alley et al., 2015).

Jacobs et al. (1996) first observed modified CDW on the continental shelf in the Amundsen Sea embayment (Figure 1) near the Pine Island Glacier ice shelf in 1994. Ensuing research has shown that the amount of warm CDW on the continental shelf in this region is sensitive to regional atmospheric variability, specifically changes to the coastal easterly wind stress (Thoma et al., 2008). These surface wind stress changes modify the Antarctic Slope Front (Jacobs, 1991), which is characterized by downward sloping isopycnals below the surface waters

that separate the relatively warm and saline CDW from the cold and fresh shelf waters. The slope of the isopycnals, and thus the strength of the lateral density gradient and barrier between the warm waters and the ice shelves, is largely controlled by the coastal easterly winds (Whitworth et al., 1998). Weaker coastal easterlies decrease Ekman downwelling near the coast, weaken the Antarctic Slope Front, and shoal the pycnocline at the shelf break creating a shoreward pathway for CDW transport and the warming of the shelf waters (Thompson et al., 2014; Spence et al., 2014; Stewart and Thompson, 2015).

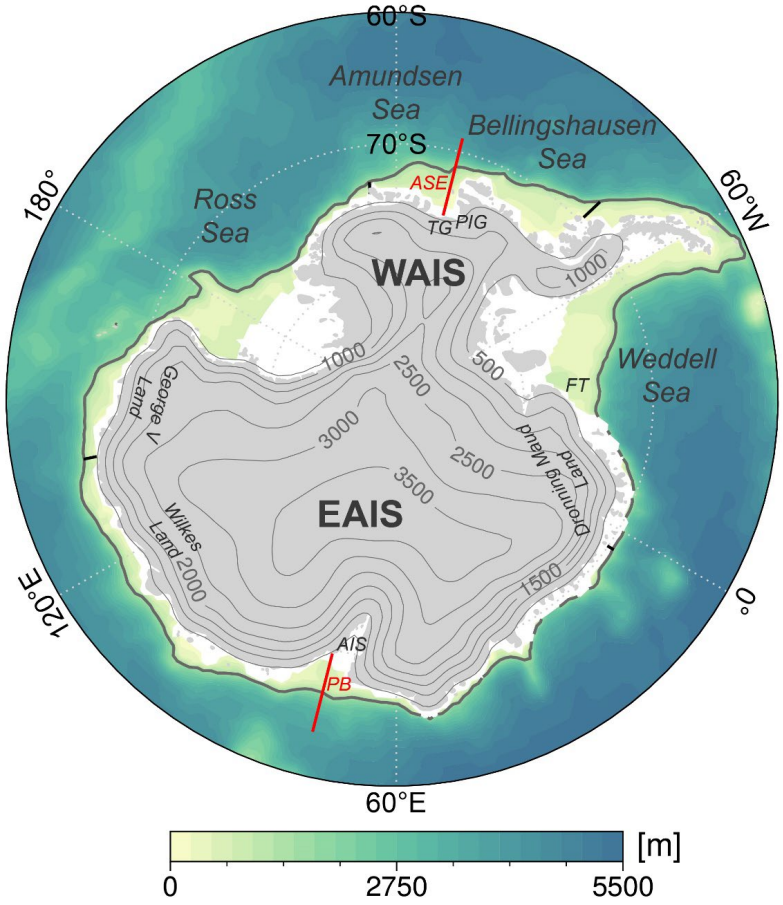

Figure 1. Ocean depth and Antarctic topography map with relevant geographic features labeled. The thick gray contour, representing the 1,500 m isobath, shows the approximate location of the continental shelf break. The thin gray topography contours are at every 500 m. The red lines show the location of cross-shelf ocean profiles in the Amundsen Sea embayment (ASE) and Prydz Bay (PB) analyzed later in the text. The black lines above the shelf waters locate the boundaries of the Amundsen Sea-Bellingshausen Sea sector and the eastern Antarctic sector used in the vertical temperature advection analysis. WAIS = West Antarctic Ice Sheet, EAIS = East Antarctic Ice Sheet, TG = Thwaites Glacier, PIG = Pine Island Glacier, AIS = Amery Ice Shelf, FT = Filchner Trough.

In the Amundsen Sea embayment, coastal wind stress changes are controlled by the strength and position of the Amundsen Sea Low (ASL, Hosking et al., 2013, 2016; Turner et al., 2013; Raphael et al., 2016), which is influenced by the variability in both the Southern Annular

Mode (SAM) and in the tropical Pacific sea surface temperatures (e.g., Ding et al., 2011; Steig et al., 2012; Clem et al., 2017). Notably, as the ASL strengthens (a reduction in sea level pressure), easterly winds increase at the shelf break which in turn strengthen the Slope Front and restrict the shoreward CDW transport; conversely, a weak ASL (an increase in sea level pressure) drives anomalous westerly winds at the shelf break which may lead to shelf warming (Dinniman et al., 2011; Spence et al., 2014; Donat-Magnin et al., 2017). Furthermore, ASL longitudinal positional shifts will alter zonal winds above the continental shelf with implications for shelf ocean warming. It should also be noted that changes in the strength and position of the cyclonic ASL can drive opposing impacts with regards to the ice shelves in the adjacent Bellingshausen Sea as compared to the Amundsen Sea, as the ASL's center often resides between the two Seas (Figure 1) (Dotto et al., 2020; Verfaillie et al., 2022).

Beyond the Amundsen-Bellingshausen Seas, SAM-related wind anomalies also influence shelf warming across East Antarctica. During the austral summer, positive SAM drives a southward shift of the mid-latitude westerly winds, a weakening of the coastal easterly winds, and a poleward migration of the southern boundary of the Antarctic Circumpolar Current; the latter induces CDW warming at the continental shelf slope, particularly in the Indian Ocean sector of East Antarctica (~110-150°E, Figure 1) (Yamazaki et al., 2021; Herraiz-Borreguero and Naveira Garabato, 2022). This mechanism may be responsible for the increased ice mass loss from this region observed this century (Greenbaum et al., 2015; Rignot et al., 2019; Smith et al., 2020). Furthermore, the SAM is projected to become more positive through the 21st century due to continued greenhouse gas emissions (Zheng et al., 2013; Coburn and Pryor, 2023), although an opposing effect from the long-term stratospheric ozone recovery can significantly offset the positive SAM trend from greenhouse gas emissions, in particularly during the early part of the 21st century and during certain seasons (austral spring and summer, Perlwitz, 2011; Thompson et al., 2011). A positive SAM trend would lead to the Westerlies expanding southward, a weakening of the coastal easterlies, and subsequent Antarctic shelf warming, including warming around East Antarctica (Spence et al., 2014; Goddard et al., 2017; Beadling et al., 2022).

Although the majority of current Antarctic ice mass loss is related to the increased basal melt and calving rates of the ice shelves, surface melt is increasingly becoming a significant contributor to Antarctic mass loss (DeConto and Pollard, 2016; Golledge et al., 2019). By the end of the 21st century, surface melt rates across Antarctica could equal that of Greenland from

early this century under the Representative Concentration Pathway 8.5 (RCP8.5) forcing (~600 Gt yr^{-1}; Trusel et al., 2015). Furthermore, increased meltwater on ice shelves may lead to increased hydrofracturing and calving rates (Scambos et al., 2009; Trusel et al., 2015; DeConto and Pollard, 2016). Surface melt rates around the Antarctic periphery have been shown to modulate with phases of SAM and the El Niño Southern Oscillation (ENSO). Many ice shelves along East Antarctica (in the Dronning Maud Land, Amery and Wilkes Land, and the Ross Sea sector of West Antarctica, Figure 1) show a negative correlation between melt days and the spring-summer SAM index (Johnson et al., 2022). Whereas melt days for ice shelves along the Amundsen Sea and eastern Ross Sea sector show a positive correlation with the spring-summer ENSO index (Scott et al., 2019; Johnson et al., 2022).

Opposingly, snow accumulation on Antarctica is projected to increase in the 21st century, acting to partially offset the mass loss from increased ocean thermal forcing and surface melt (Payne et al., 2021). Many regions inland from the coast receive a large proportion (~40-60%) of their annual precipitation during infrequent but extreme events characteristic of atmospheric rivers (ARs) (Schlosser et al., 2010; Turner et al., 2019; Wille et al., 2021; Davison et al., 2023). These events bring relatively warm and moist maritime air to the Antarctic interior, driving surface snow accumulation in both West Antarctica and East Antarctica. For example, Adusumilli et al. (2021) attributes the rapid increase in surface height of the West Antarctic Ice Sheet in 2019 to AR-induced precipitation from a deepening and westward shift of the ASL. This result is consistent with the findings of Maclennan and Lenaerts (2021) that show a blocking high over the Antarctic Peninsula tends to contribute to large snowfall events over the Thwaites Glacier from 1980-2015. Wille et al. (2021) finds a significant positive correlation between the SAM and AR events on the Antarctic Peninsula and a significant negative correlation between the SAM and AR events across West Antarctica. AR events around East Antarctica are also associated with blocking anticyclones and an amplification of Rossby waves which bring low latitude moisture to the continent (Schlosser et al., 2010; Gorodetskaya et al., 2014; Maclennan et al., 2022). Finally, over the 21st century ARs are projected to increase in duration and strength (quantified by integrated vapor transport) due to a warmer atmosphere's capacity to hold more moisture (Espinoza et al., 2018; Payne et al., 2020; O'Brien et al., 2022).

Despite the projected increase in Antarctic snow accumulation, under RCP8.5 forcing, sea level rise contributions from Antarctica are projected to increase and to surpass Greenland by

the year 2100 (with the upper end of the likely contribution being ~0.3 m above the 1986-2005 mean; IPCC, 2019). Research also suggests that the West Antarctic Ice Sheet is susceptible to self-perpetuating collapse if global mean temperatures pass ~1.5°C above pre-industrial levels (Armstrong McKay et al., 2022). It is therefore prudent to research the Antarctic climate response and projected ice loss in SAI cases where global mean warming is kept below 1.5°C. However, the only previous study explicitly examining SAI impacts on the Antarctic region, McCusker et al. (2015), shows that an 8 Tg yr^{-1} sulfate aerosol addition between 10°S and 10°N beginning in 2035 (increasing by 0.67 Tg yr^{-1} after 2037 to continue to offset the RCP8.5 radiative forcing) will still lead to warming of the subsurface Antarctic shelf waters around the mid-21st century (albeit less warming than the RCP8.5 scenario alone) despite cooling mid-21st century global mean surface air temperature to the late-20th century level. The authors focus on the Amundsen Sea embayment and attribute the persistent shelf ocean warming at depth to the equatorial sulfate injection disrupting the upper troposphere/lower stratosphere meridional temperature gradients, thereby leading to a weakening of the coastal easterlies and increased Ekman upwelling of the relatively warm CDW onto the shelf.

More recently, Bednarz et al. (2022) shows that while deploying SAI at the Equator or in the northern hemisphere will indeed induce similar weakening of the coastal easterlies as found in McCusker et al. (2015), injecting in the southern hemisphere will strengthen coastal easterlies relative to a mid-century SSP2-4.5 scenario. Specifically, Bednarz et al. (2022) finds that injecting 12 Tg-SO_2 yr^{-1} at the Equator, 15°N, or 30°N will shift the southern hemisphere tropospheric eddy-driven jet poleward resulting in sea level pressure and wind patterns consistent with a positive phase of SAM, while injecting at 15°S or 30°S will shift the eddy-driven jet equatorward resulting in patterns consistent with a negative phase SAM. This opposing impact of SAI on Antarctic regional atmospheric conditions and circulation with respect to the hemisphere of aerosol injection motivates the current study. Here we use a comprehensive set of seven single-latitude injection sensitivity simulations and four more complex multiple-latitude injection cases to systematically analyze the following questions: How do various SAI cases impact the SAM and ASL variability (Section 3.1)? Which SAI cases lead to warmer surface air temperature or greater precipitation above the continent relevant to surface mass balance (Sections 3.1 and 4.1)? Finally, which SAI cases lead to continued upwelling of warm water on the Antarctic continental shelf (Sections 3.2 and 4.1)?

2 Model and Methods

In this work we consider eleven SAI cases (Table 1) simulated using the Community Earth System Model (CESM) version 2, using the Whole Atmosphere Community Climate Model version 6 as the atmospheric component (CESM2-WACCM6; Gettelman et al., 2019; Danabasoglu et al., 2020). The atmospheric horizontal resolution is 1.25° longitude by 0.95° latitude, with 70 vertical layers extending from the surface to about 140 km. The simulations use the Middle Atmosphere chemistry configuration (Davis et al., 2022) that includes an interactive stratospheric and upper atmospheric chemistry in addition to aerosol microphysics from the Modal Aerosol Module (MAM4; Liu et al., 2016). The ocean model (Parallel Ocean Program Version 2) horizontal resolution is 1.125° in the zonal direction and ranges between about 0.27° and 0.64° in the meridional direction and includes 60 vertical levels (Smith et al., 2010; Danabasoglu et al., 2012). There is not a coupled dynamic Antarctic ice sheet model in our simulations and as such basal melt is not represented. However, here we use the shelf ocean warming as a proxy for basal melt. The simulations use the coupled Land Model version 5.0 (Lawrence et al., 2019) to track ice accumulation (via precipitation), calving, and liquid runoff. In the current simulation design, the rates of calving and liquid runoff to the nearby ocean are defined as to offset the ice accumulation above that Antarctic surface, such that when integrated across space and time the surface mass balance is in equilibrium and topography is stationary. Each SAI case is simulated using the background CMIP6 SSP2-4.5 scenario (Meinshausen et al., 2018; Meinshausen et al., 2020) with the sulfate precursor (SO_2) injection beginning in January 2035 and continuing through December 2069.

Table 1. A summary of the eleven SAI cases and the Historical and SSP2-4.5 simulations including the number of ensember members, latitude(s) of injection, the season(s) or year-round application of the injection, the approximate amount of injection averaged during 2050-2069 in Tg-SO_2 yr^{-1}, the analysis time period, and the global mean temperature response during this time period relative to the pre-industrial time period (± 1 standard error, where the sample size is the number of years across all ensemble members). The simulation name is in italics if their results are located in the Supporting Information.

Sim. Abbr.	Ens. Mem.	Latitude of Inj.	Ann. or Seas.	Tg-SO_2 yr^{-1}	Analysis	GMT - PI (°C)
HIST	3	N/A	N/A	N/A	1990-2009	0.6 ± 0.1
SSP2-4.5	3	N/A	N/A	N/A	2050-2069	2.4 ± 0.1
30N-ANN	2	30°N	ANN	12.0	2050-2069	1.4 ± 0.1
15N-ANN	2	15°N	ANN	12.0	2050-2069	1.5 ± 0.1
EQ-ANN	2	Equator	ANN	12.0	2050-2069	1.6 ± 0.1
15S-ANN	2	15°S	ANN	12.0	2050-2069	1.4 ± 0.1
30S-ANN	2	30°S	ANN	12.0	2050-2069	1.3 ± 0.1

60S-SON	1	60°S	SON	12.0	2050-2069	1.6 ± 0.1
60N-MAM	1	60°N	MAM	12.0	2050-2069	1.7 ± 0.1
Global+1.5	3	30°N, 15°N, 15°S, 30°S	ANN	8.6	2050-2069	1.6 ± 0.1
Global+1.0	3	30°N, 15°N, 15°S, 30°S	ANN	17.0	2050-2069	1.0 ± 0.1
Global+0.5	3	30°N, 15°N, 15°S, 30°S	ANN	25.6	2050-2069	0.6 ± 0.1
Polar+1.0	3	60°N, 60°S	MAM, SON	20.4	2050-2069	1.2 ± 0.1

The first set of SAI cases, consisting of seven simulation setups, each inject SO_2 at every timestep at a single latitude into the lower stratosphere at a constant rate equivalent to 12 Tg-SO_2 per year (Table 1). The first five of these simulations, which inject SO_2 year-round at ~21.5 km altitude and either at 30°N, 15°N, 0°N, 15°S, or 30°S, respectively, were introduced in Visioni et al. (2023) and Bednarz et al. (2023) and used to examine the response of the SAM to SAI in Bednarz et al. (2022). Additionally, we introduce two other single-latitude injection cases that inject at 60°S during the austral spring (SON) or at 60°N during the boreal spring (MAM) at about 15 km in altitude. These six SAI cases will be abbreviated as 60N-MAM, 30N-ANN, 15N-ANN, EQ-ANN, 15S-ANN, 30S-ANN, and 60S-SON.

The second set of SAI cases, consisting of four more complex simulation setups, each inject SO_2 at every timestep at multiple latitudes simultaneously and under time-varying injection rates (Table 1). The injection rates are determined at the beginning of each year by a feedback algorithm such as to maintain the annual global mean near-surface temperature (GMT) at a chosen level above the pre-industrial (PI) conditions. Three of these simulations, introduced in MacMartin, et al. (2022), each inject at 30°N, 15°N, 15°S, and 30°S to maintain GMT at 1.5°C + PI, 1.0°C + PI, and 0.5°C + PI, respectively. After slowly increasing SAI rates to meet the GMT goals, the GMT for years 2050-2069 in these simulations have the same GMT as years 2020-2039, 2008-2027, and 1993-2012 from the CESM2-WACCM6 SSP2-4.5 and/or historical forcing simulations, respectively. These SAI cases also meet two other objectives: maintaining the interhemispheric surface temperature gradient and the Equator-to-pole surface temperature gradient at their reference PI levels as detailed in Kravitz et al. (2017) and Tilmes et al. (2018). Additionally, we introduce a fourth multi-latitude injection case that injects at 60°S during austral Spring (SON) and 60°N during boreal Spring (MAM) to meet the 1.0°C + PI GMT objective (Zhang et al., 2023). These four SAI cases will be abbreviated as Global+1.5, Global+1.0, Global+0.5, and Polar+1.0. For these cases, the total amount of SO_2 injected per

year averaged for years 2050-2069 is about 8.6, 17.0, 25.6, and 20.4 Tg-SO_2 yr^{-1}, respectively (Visioni et al., *submitted*; Zhang et al., 2023).

The two different sets of SAI cases serve two complementary purposes. The single-latitude injection cases, with a fixed amount injected per year, serve to more easily diagnose changes to the climate system by considering one location at a time. Their purpose is not to illustrate a desirable deployment strategy; rather, they serve as a 'step-function' response which can inform more complex strategies that rely on a combination of multiple injection locations and use time-varying injection rates to maintain one or more climate targets, assuming a certain linearity of the system and additivity between different locations *(*Visioni et al., *submitted)*. Bednarz et al. (2022) showed the potential of these single-latitude injection simulations to explore physical mechanisms driving the SAI responses and to explain changes in another set of multi-latitude injection simulations for one particular climate driver, the Southern Annular Mode. Finally, comparisons between the Global+1.5, Global+1.0, Global+0.5 simulations allow one to ascertain to which degree the observed changes depend on the amount of GMT cooling obtained, while comparisons between Global+1.0 and Polar+1.0 allow a comparison of two strategies with similar GMT, but different injection strategies. All eleven SAI cases are summarized in Table 1, including the number of ensemble members for each strategy.

Here, we analyze the ensemble mean results from the last 20 years of the SAI simulations (2050-2069) and compare them to CESM2-WACCM6 simulations of the CMIP6 historical forcing near the turn of the 21st century (1990-2009). We contrast these responses with the analogous responses simulated in the CESM2-WAACM6 CMIP6 SSP2-4.5 simulations as a control greenhouse gas scenario without SAI for the same time period (2050-2069). We denote a statistically significant change where the difference in the two means is greater than ±2 standard errors. The sample size is the number of years across all ensemble members and is adjusted depending upon the autocorrelation at each model grid box, where necessary (Wilks, 1997).

3 Results

3.1 Antarctic surface climate

In addition to reflecting incoming solar radiation, the injected aerosols will also absorb some incoming solar radiation which in turn warms the lower stratosphere. This localized warming with respect to the Historical simulation (1990-2009) is shown in the first two columns

of Figure 2. Consistent with the results of Bednarz et al. (2022), this warming strengthens the stratospheric Equator-to-pole temperature gradient initiating a year-round strengthening of the stratospheric polar jet (Figure 2 – last column). This dynamical response also alters tropospheric circulation expressed through latitudinal shifts and/or strength modification of the tropospheric eddy-driven jet. Of particular importance to the current study, in the southern hemisphere (SH) these anomalies differ in sign and magnitude depending on the latitude(s) of the injection. The single-latitude injection cases at the Equator (EQ-ANN), 15°N (15N-ANN, Figure S1), or 30°N (30N-ANN) shift the SH eddy driven jet poleward, whereas injection cases at 15°S (15S-ANN, Figure S1) or 30°S (30S-ANN) shift the tropospheric jet Equatorward. Furthermore, these circulation anomalies reach the surface at about 60°S and are expressed as westerly anomalies for the Equator and northern hemisphere (NH) injection cases and easterly anomalies (or no significant change) for SH injection cases. As described in Bednarz et al. (2022) these opposite responses at the surface are linked to associated changes in the tropospheric eddy heat and momentum fluxes as well as stratospheric wave propagation or breaking and high latitude downwelling during austral winter and spring.

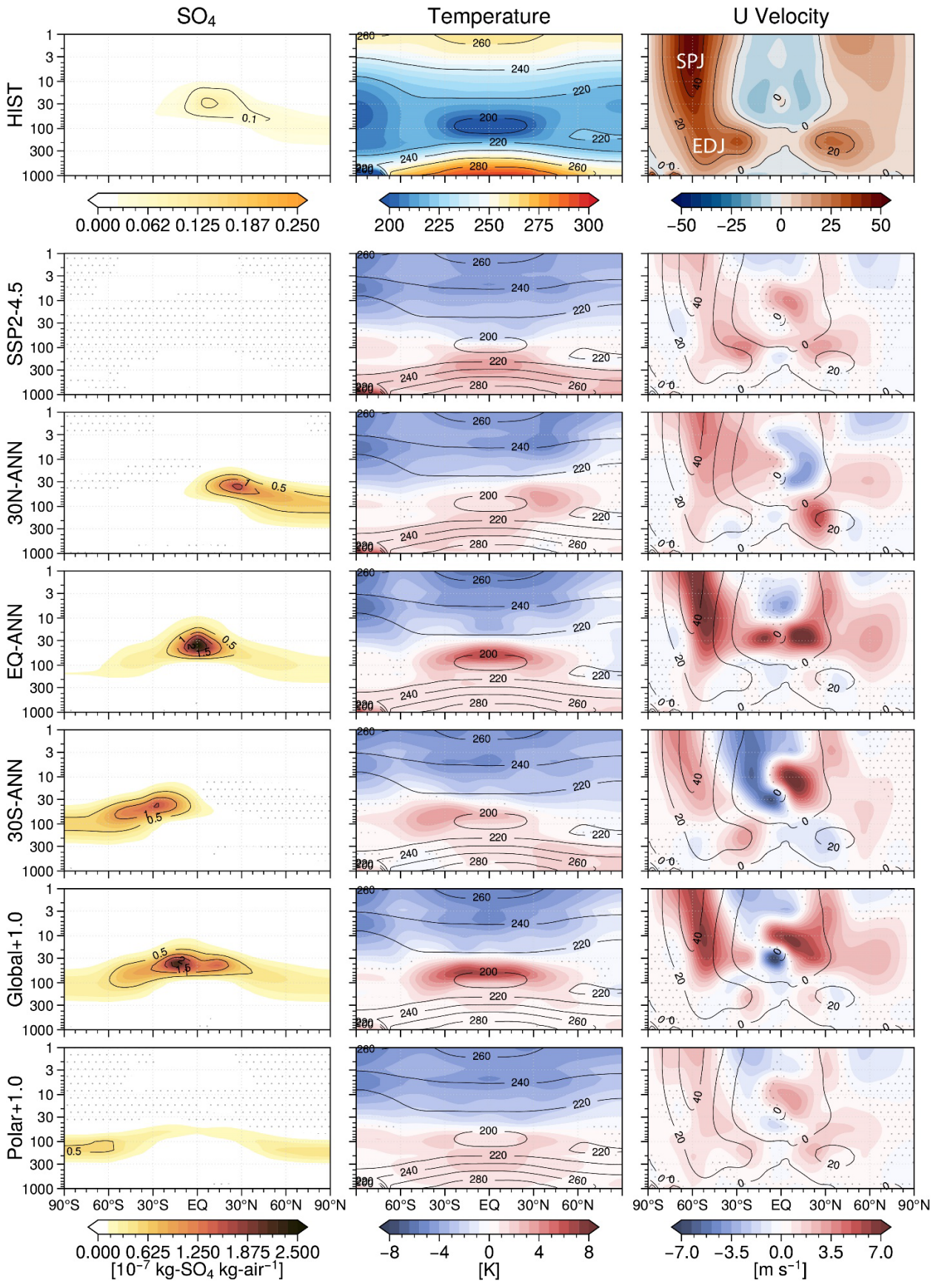
SO4
Temperature
U Velocity
HIST
SSP2-4.5
30N-ANN
EQ-ANN
30S-ANN
Global+1.0
Polar+1.0
SPJ
EDJ
0.000 0.062 0.125 0.187 0.250
200 225 250 275 300
−50 −25 0 25 50
90°S 60°S 30°S EQ 30°N 60°N 90°N
0.000 0.625 1.250 1.875 2.500
[10−7 kg-SO4 kg-air−1]
−8 −4 0 4 8
[K]
−7.0 −3.5 0.0 3.5 7.0
[m s−1]

293

Figure 2. The top row shows the Historical annual ensemble mean (1990-2009) zonal mean sulfate burden (10^{-7} kg-SO_4 kg-air^{-1}), temperature (K), and zonal wind velocity (m s^{-1}). Shading in the following rows show the annual ensemble mean anomalies (2050-2069) from the Historical with respect to SSP2-4.5 and the SAI cases. Contours in the first column show the sulfate burden difference from the Historical, whereas, in columns two and three, contours show the corresponding temperatures and zonal velocity in the Historical simulation for reference. Stippling shows the regions where the difference is not statistically significant. SPJ = southern hemisphere stratospheric polar jet; EDJ = southern hemisphere eddy-driven jet.

The single-latitude injection cases also reveal that the Equator and NH single-latitude injections drive year-round sea level pressure (SLP) reductions above Antarctica and westerly surface wind stress anomalies around the coastline consistent with a positive phase of SAM (Figures 3 and S2). These anomalies are similar in pattern and larger in magnitude as compared to the SSP2-4.5 anomalies which also reflect a positive SAM and are consistent with previous studies projecting a positive trending SAM through the 21st century under greenhouse gas forcing (Zheng et al., 2013; Coburn and Pryor, 2023). Conversely, SH single-latitude injections drive anomaly fields consistent with a negative SAM (pressure increases and easterly wind anomalies above and around Antarctica).

Analyzing the surface wind stress and SLP anomalies resulting from the single-latitude injection cases can help interpret the results from the multi-latitude injection cases: Global+1.0 and Polar+1.0 (with Global+0.5 and Global+1.5 shown in the Supporting Information). The Global+1.0 case shows that the westerly anomalies derived from the stratospheric polar jet strengthening do not propagate down to the troposphere and modify the tropospheric jet nor drive westerly anomalies at the surface at 60°S (Figure 2 - last column). Therefore, the circumpolar wind stress and SLP anomalies do not reflect a characteristic positive SAM phase that one would expect under the strengthening of the stratospheric jet. Instead, the anomalous SLP dipole off the coast of West Antarctica and the Peninsula is consistent with the Pacific-South American (PSA) pattern that represents an Equator-to-pole atmospheric Rossby wave response to changes in central tropical Pacific sea surface temperature (Kidson, 1998; Mo and Higgins 1998; Yiu and Maycock, 2019). This PSA pattern is associated with longitudinal shifts in the Amundsen Sea Low wherein positive central Pacific sea surface temperature anomalies are associated with a blocking high over the Antarctic Peninsula and a westward migration of the ASL (Figure 3) (Ding et al., 2011; Goddard et al., 2021). This PSA teleconnection is less prominent for SAI cases that strengthen the SH eddy-driven jet as this frontal enhancement

reflects or breaks the Rossby wave train before reaching the Amundsen-Bellingshausen Seas region (Schneider et al., 2012; Yiu and Maycock, 2019).

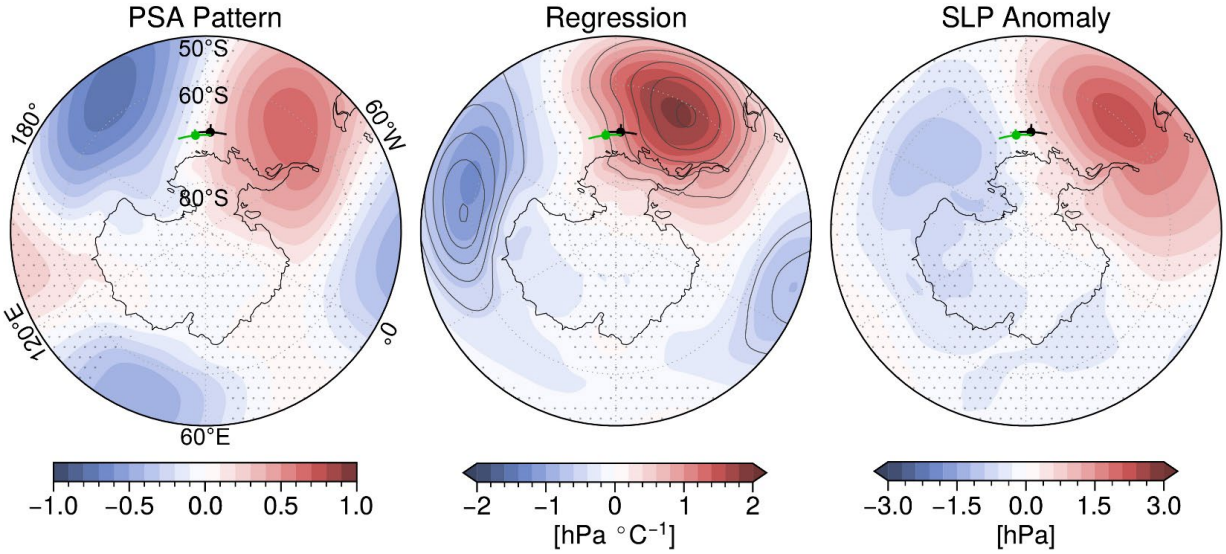

Figure 3. The left panel shows the Pacific-South American pattern defined from the standardized leading modes of variability from an empirical orthogonal function analysis of the Historical (1990-2009) area-weighted monthly mean sea level pressure anomalies with respect to its climatology poleward of 20°S (Yu et al., 2012). The pattern shown accounts for 11.4 ± 0.2% (±1 σ with respect to the ensemble members) of the variability in the anomalous SLP field (the SAM pattern accounts for 26.5 ± 1.8% and the other Pacific-South American pattern (associated with the depth of the Amundsen Sea Low) accounts for 9.4 ± 0.7%). The center panel shows the linear regression slope of Global+1.0 (2050-2069) monthly SLP anomalies from the Historical onto the Global+1.0 monthly central Pacific (5°S:5°N & 160°E:30°W average) sea surface temperature anomalies from the Historical. The contours show the explained variance (contours begin at 5% and increase by 5% per level). The right panel shows the annual ensemble mean anomalies of Global+1.0 from the Historical ensemble mean sea level pressure (hPa). In all panels, the center of the green cross marks the annual mean location of the Historical ASL position, and the black cross marks the Global+1.0 ASL position, with ±1 standard deviation in the longitudinal and latitudinal directions (crosses). Stippling shows the regions where the values are not statistically significant.

The Polar+1.0 surface wind stress and SLP anomalies can also be interpreted through the analysis of the single-latitude injection simulations. Both 30S-ANN (significant change) and 15S-ANN (non-significant) show easterly anomalies in the annual zonal mean velocity at the surface at 60°S (Figures 2 and S1). However, in 60S-SON this anomaly is weakly westerly (non-significant, Figure S1). This anomaly is, at least in part, due to the preferential cooling of the SH high latitudes and relative warming of the mid-to-low latitudes which enhances the tropospheric meridional temperature gradient and results in increased westerly winds at the surface. Furthermore, in addition to injecting at 60°S in austral spring, the Polar+1.0 simulation also injects at 60°N in boreal spring (MAM). Consistent with the 15N-ANN and 30N-ANN responses, 60N-MAM strengthens the tropospheric polar jet resulting in significant westerly

wind anomalies at the surface near 60°S (Figures S1 & S2). Therefore, the combination of injecting at both 60°S and 60°N as the Polar+1.0 case does, results in a significant annual mean westerly anomaly at the surface at 60°S (Figure 2). The surface wind stress and SLP anomaly fields are in turn consistent with a positive SAM (Figure 4). In summary, both Global+1.0 and Polar+1.0 similarly reduce global mean temperature relative to the pre-industrial while the different injection distribution drives different dynamical responses that lead to different circulation patterns around Antarctica.

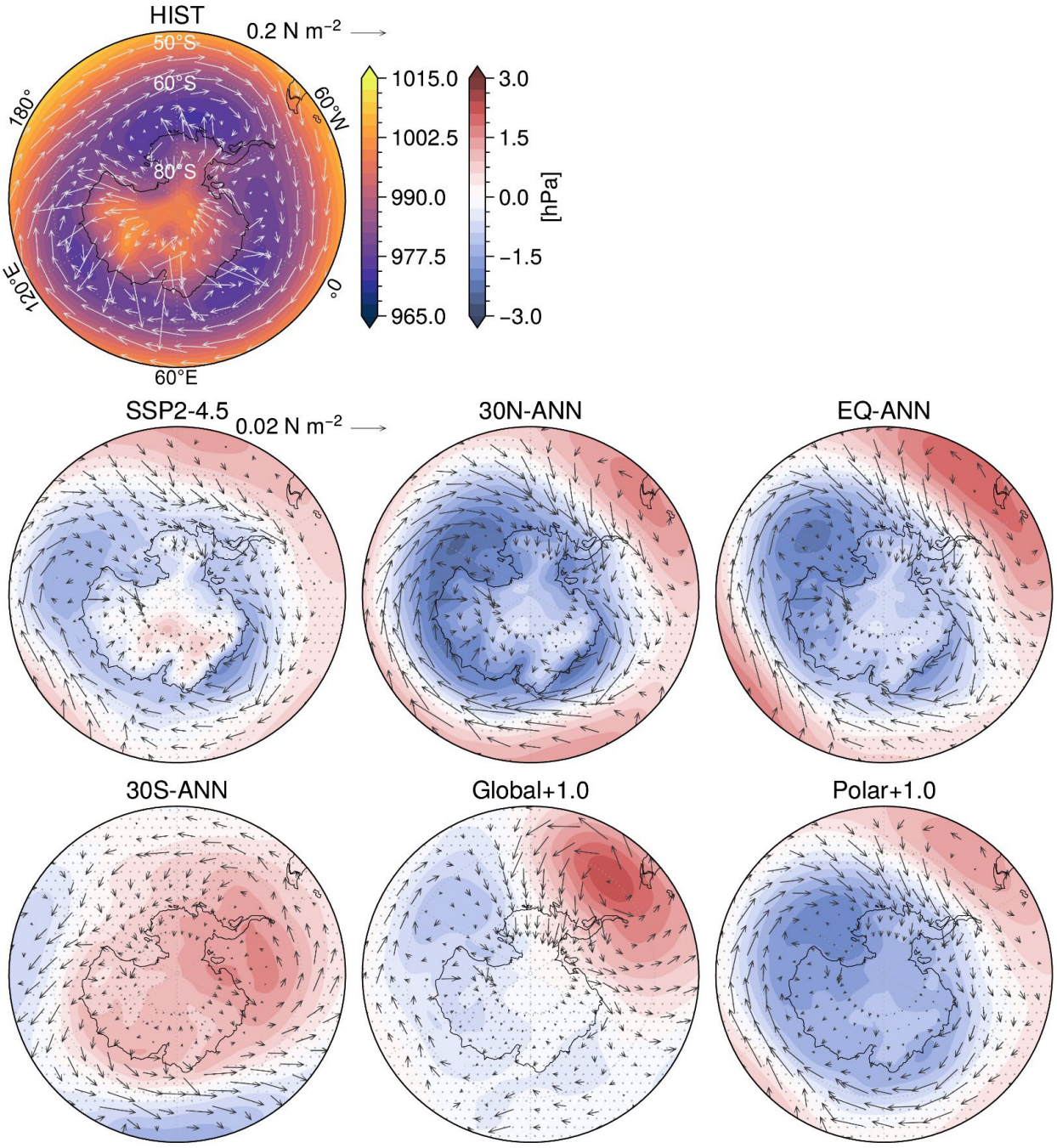

Figure 4. The top left panel shows the Historical annual ensemble mean (1990-2009) sea level pressure (hPa) and surface wind stress vectors (N m^{-2}, in the direction of the surface winds). The following rows show the annual ensemble mean anomalies (2050-2069) from the Historical with respect to SSP2-4.5 and the SAI cases. Stippling shows the regions where the sea level pressure difference is not statistically significant.

For each SAI case, the circulation changes will drive surface air temperature (SAT) and precipitation anomalies around Antarctica. To first order these anomalies respond to hemispheric-scale temperature changes that differ with respect to each SAI case. The annual

mean change in SAT poleward of 50°S with respect to the Historical simulation is +1.7° (SSP2-4.5), +1.5° (30N-ANN), +1.0° (EQ-ANN), -0.2° (30S-ANN), +0.4° (Global+1.0), and +0.3°C (Polar+1.0), where one standard error of the difference in means is about 0.05°C. (For context, the corresponding temperature in years 2008-2027 from the SSP2-4.5 simulation where the global mean temperature was the same as in Global+1.0 and Polar+1.0 was +0.4°C; the polar strategy indeed focuses more cooling on the high-latitude regions relative to the global mean.) As expected, the cases which inject the least SO_2 in the SH cool SAT in the Antarctic region the least, leaving residual warming as the impact of increasing greenhouse gases is not being fully offset (Figure 5). Consistent across all cases except for 30S-ANN and 60S-SON (Figure S3), the positive SAT anomalies over the ocean are greatest across the eastern Amundsen Sea to the Antarctic Peninsula and between about 20°E and 50°E. These locations are associated with wind anomalies that have a northerly component which not only transports warmer air from lower latitudes to the area but also contributes to the reduced local sea ice extent (Figure 5 – contours). Regarding each case, SAT anomalies over the continent vary less than the anomalies over the nearby ocean, with the largest residual warming relative to the Historical typically located on the Antarctic Peninsula and over West Antarctica.

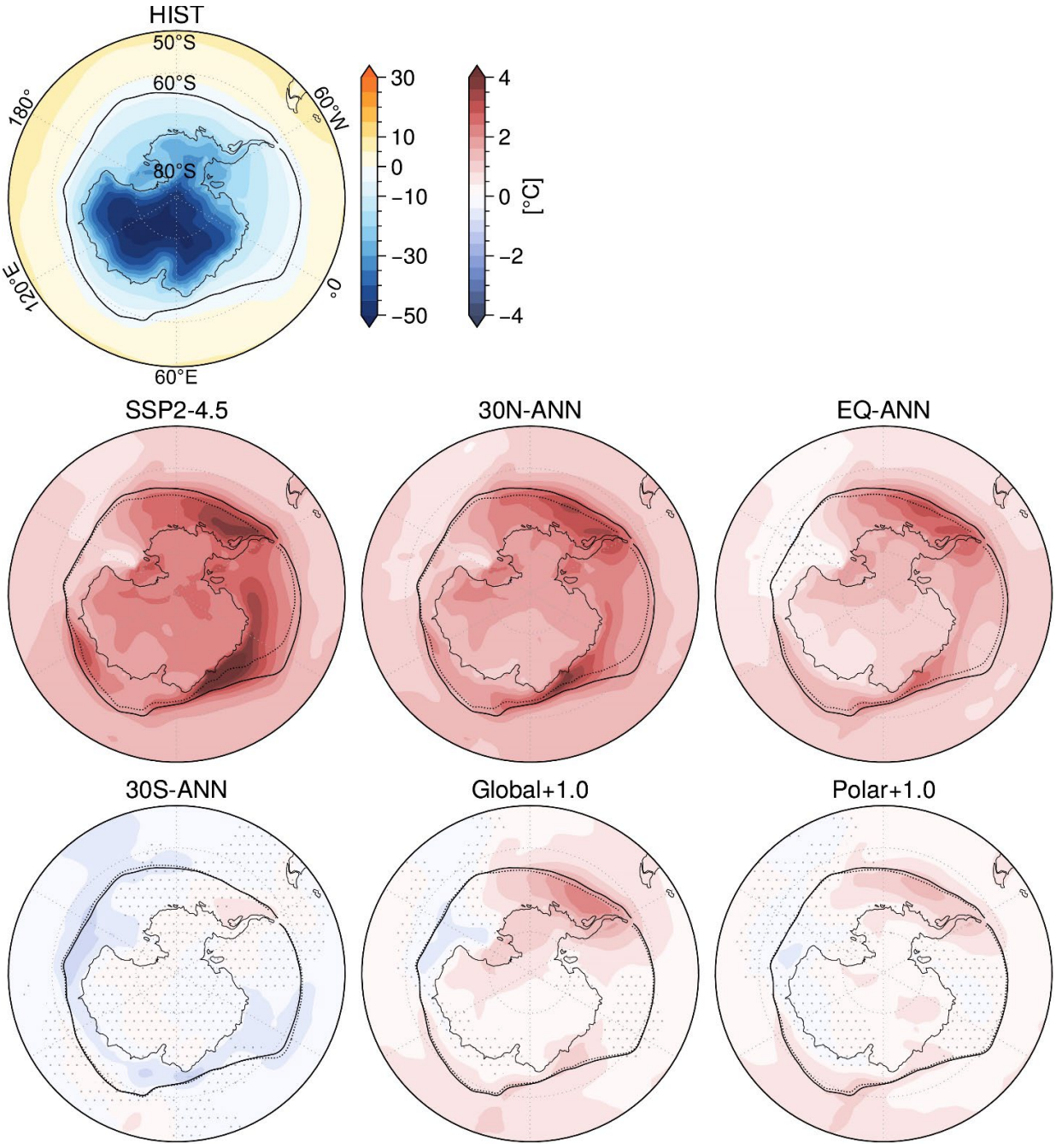

Figure 5. The top left panel shows the Historical annual ensemble mean (1990-2009) surface air temperature (SAT, °C) with a solid black contour showing the sea ice extent (at 25% concentration). Shading in the following rows show the annual ensemble mean SAT anomalies (2050-2069) from the Historical with respect to SSP2-4.5 and the SAI cases. Each of these panels show the Historical sea ice extent contour (solid) and the SSP2-4.5 or SAI case contour (dashed). Stippling shows the regions where the SAT difference is not statistically significant.

Similarly, total precipitation anomalies over Antarctica are primarily associated with the changing moisture capacity of the atmosphere. The annual mean 50°S-to-pole total precipitable

water anomaly with respect to the historical simulation is +1.0 (SSP2-4.5), +0.8 (30N-ANN), +0.6 (EQ-ANN), -0.1 (30S-ANN), +0.2 (Global+1.0), and +0.3 kg m^{-2} (Polar+1.0), where one standard error of the difference in means is about 0.03 kg m^{-2} (Figure 6 - contours). Superimposed upon these mean changes in total precipitable water, the circulation anomalies drive significant regional increases in precipitation along the coast of West Antarctica, the Peninsula, and between about 0°E and 60°E in East Antarctica (Figures 6 and S4). The positive precipitation anomaly towards the tip of the Peninsula and between 0°E and 60°E in the Equator, NH, and Polar+1.0 cases is due to the westerly storm track migrating southward associated with the positive SAM conditions (Wille et al., 2021), whereas, the precipitation increase in West Antarctica is due to the westward migration of the ASL and the positive pressure anomaly near the Peninsula associated with the PSA pattern (Figure 4) (Adusumilli et al., 2021; Maclennan and Lenaerts; 2021). These PSA-associated SLP anomalies are most prominent in Global+1.0 and set up a moisture pathway from the lower latitudes to the interior of West Antarctica (similarly as is the case for Global+1.5 and Global+1.0, Figures S2 and S4). In the SH single-latitude injection cases, changes to precipitation around the Antarctic periphery are very small and often non-significant.

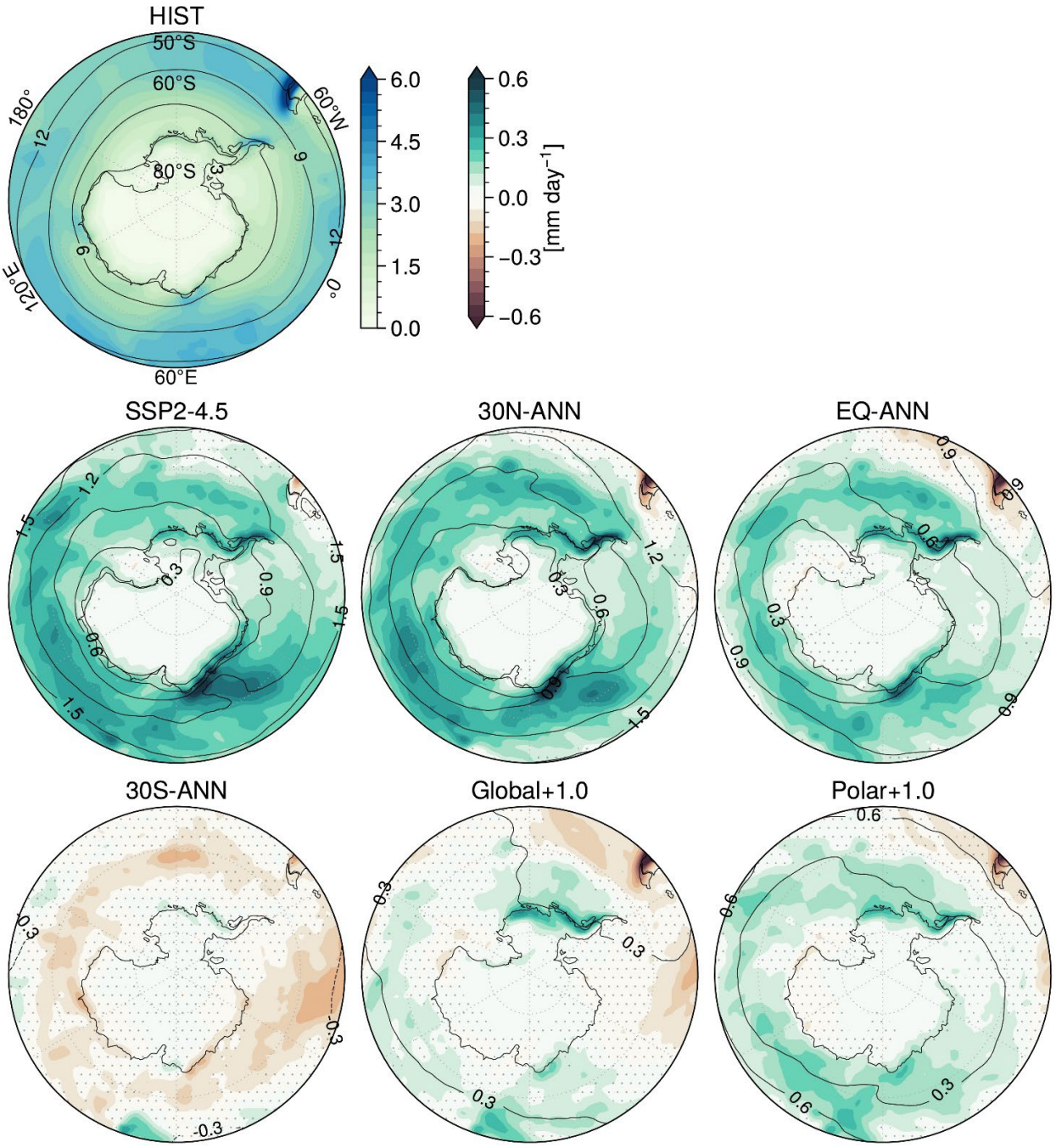

411

412 **Figure 6**. The top left panel shows the Historical annual ensemble mean (1990-2009) total precipitation
413 (mm yr^{-1}) with black contours showing total precipitable water (kg m^{-2}). Shading in the following rows
414 show the annual ensemble mean total precipitation anomalies with black contours showing total
415 precipitable water anomalies (2050-2069) from the Historical with respect to SSP2-4.5 and the SAI cases.
416 Stippling shows the regions where the total precipitation difference is not statistically significant.

417 Combining the changes to SAT and precipitation over Antarctica, we can assess changes
418 to surface ice accumulation for each SAI case. In the Historical simulation, only at the northern
419 tip of the Peninsula is the amount of surface ice melt greater than ice formation resulting from

precipitation (Figure 7). Across the rest of Antarctica there is an annual mean gain in surface ice mass. With respect to the Historical, the SAI surface accumulation anomalies are very similar to the anomalous precipitation patterns (Figures 6-7 and S4-S5). The enhanced hydrological process dominates the mass gain anomalies because despite SAT increase for most SAI cases, the temperature is still below 0°C for the annual mean (Figures 5 and S3). The only exception under most SAI cases is at the northern part of the Peninsula where the SAT increases and ice formation declines relative to the Historical. The reduction in ice accumulation at this location can exceed -2.0 mm day^{-1}. Furthermore, consistent with the precipitation results, the SH single-latitude injection cases show small, and often non-significant changes to ice accumulation. In summary, the surface ice accumulation anomalies with respect to the Historical simulation are largely driven by precipitation increases due to the enhanced hydrological cycle from greenhouse warming, with regional variability consistent with changes to the SAM index or longitudinal shifts of the ASL via the PSA teleconnection.

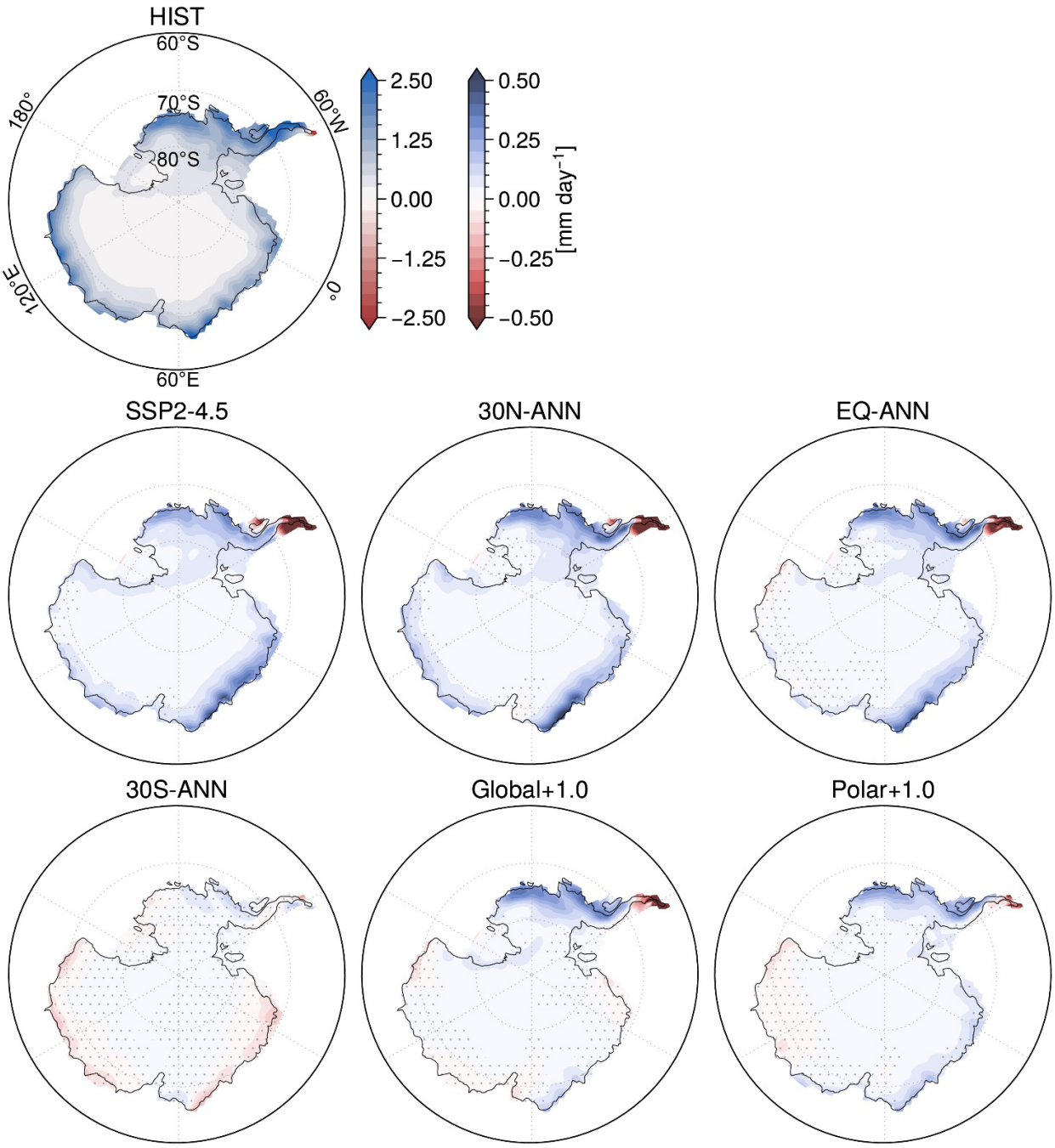

Figure 7. The top left panel shows the Historical annual ensemble mean (1990-2009) net surface ice accumulation (mm day^{-1}). Shading in the following rows show the annual ensemble mean ice accumulation anomalies (2050-2069) from the Historical with respect to SSP2-4.5 and the SAI cases. Stippling shows the regions where the accumulation difference is not statistically significant.

3.2 Antarctic shelf ocean

The Antarctic surface climate anomalies directly alter shelf ocean conditions through three surface mechanisms: surface ocean radiative flux, surface ocean momentum flux through wind stress, and surface ocean salinity flux. With regards to the first mechanism, Figure S6

shows that the largest near surface shelf ocean temperature warming (0-100 m mean) occurs near the Peninsula and along East Antarctica between about 20°E and 50°E coinciding with positive SAT temperature anomalies over these regions as shown in Figures 5 and S3. Similarly, these 0-100 m mean shelf ocean temperature anomalies are primarily driven by the mean large (hemispheric) scale SAT anomalies and the surface radiative flux response due to shifts in the SAM index. Furthermore, like the SAT anomalies, the Equator and NH single-latitude SAI cases warm these surface waters the most and the SH-only, Global+1.0, and Polar+1.0 SAI cases show minimal warming (and sometimes even significant cooling) with respect to the Historical.

Shelf ocean warming below 100 m, pertinent to ice shelf basal melt and ice sheet mass loss, is primarily driven by surface wind stress changes near Antarctica's coastline. A change to the wind stress curl, or Ekman pumping, impacts the downwelling rate of the surface waters at the ocean-ice shelf interface. When coastal easterly wind stress is robust, Ekman pumping continuously supplies cold fresh surface waters to the subsurface of the shelf ocean. However, when easterly wind stress weakens there is anomalous Ekman upwelling of the off-shelf relatively warm and saline Circumpolar Deep Water (CDW) onto the shelf where it warms the surrounding shelf waters from below. Figures 8 and S7 show that the Historical Ekman downwelling is significantly reduced (a relative Ekman upwelling anomaly) along most of the West Antarctic and East Antarctic coastline for the Equator and the NH-only SAI cases as well as SSP2-4.5. The Ekman upwelling anomalies for Global+1.0 and Polar+1.0 are comparatively lower in magnitude or non-significant in these regions. Moreover, the 30S-ANN SAI cases increases Ekman pumping along East Antarctica and the western portion of West Antarctica as a result of the increased coastal easterly wind stress, as explained in the previous Results Section and shown in Figure 4. For each respective SAI case, these changes to Ekman pumping are consistent with the associated impacts on the SAM and the resulting surface wind stress anomalies along the coast.

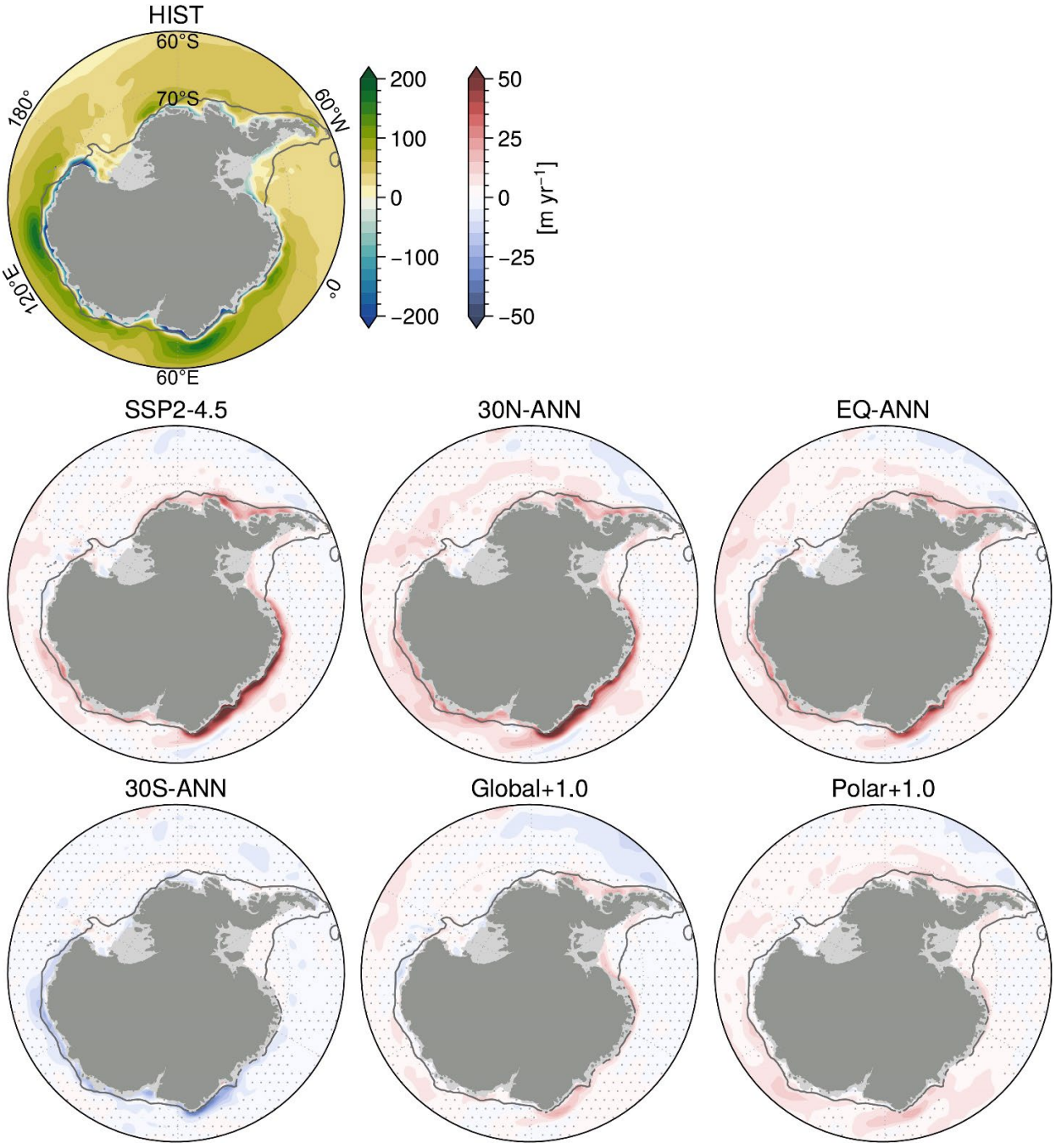

Figure 8. The top left panel shows the Historical annual ensemble mean (1990-2009) Ekman upwelling (positive values) and Ekman pumping (negative values) (m yr^{-1}). Shading in the following rows show the annual ensemble mean anomalies (2050-2069) from the Historical with respect to SSP2-4.5 and the SAI cases. Stippling shows the regions where the difference is not statistically significant. The dark gray contour follows the 1,500 m isobath.

Comparing the anomalous Ekman pumping patterns to the 100-1000 m mean shelf ocean temperature anomalies reveals a qualitative link between changes in the surface wind stress and the subsurface shelf ocean temperature (Figures 9 and S8). In general, for the equator and NH

476 SAI cases and at the locations for which coastal Ekman upwelling anomalies occur, the mean
477 subsurface shelf ocean temperature increases; and opposingly, for the SH SAI cases and
478 locations where Ekman downwelling is enhanced, the mean subsurface temperature decreases
479 relative to the Historical. An exception to this generalization is the 100-1000 m mean shelf ocean
480 warming simulated in all SAI cases in the Weddell Sea sector. The simulated Weddell Sea shelf
481 warming is likely associated with the interaction between the Filchner trough (see Figure 1) and
482 the Antarctic Slope Front and Current which reside just offshore of the shelf break (Hellmer et
483 al., 2012). The shoaling of the isopycnals in the Antarctic Slope Front near the Filchner trough in
484 response to temperature, salinity, or wind stress changes can initiate a pathway for off-shelf
485 CDW to encroach upon the shelf (Ryan et al., 2020; Bull et al., 2021). However, in a regional
486 high-resolution modeling study, Daae et al. (2020) shows that relatively severe changes to the
487 Antarctic Slope Front would need to occur for the warm water to consistently access the Weddell
488 Sea shelf. Therefore, in the current study, it is likely that the Weddell Sea shelf ocean warming is
489 an overestimate given that this response results in all SAI cases despite opposing changes to
490 surface wind stress and that many of the relevant processes occur at the subgrid scale and are
491 thus parameterized in the current simulations. Caveats concerning the ocean model's resolution
492 are further explained in the Discussion section.

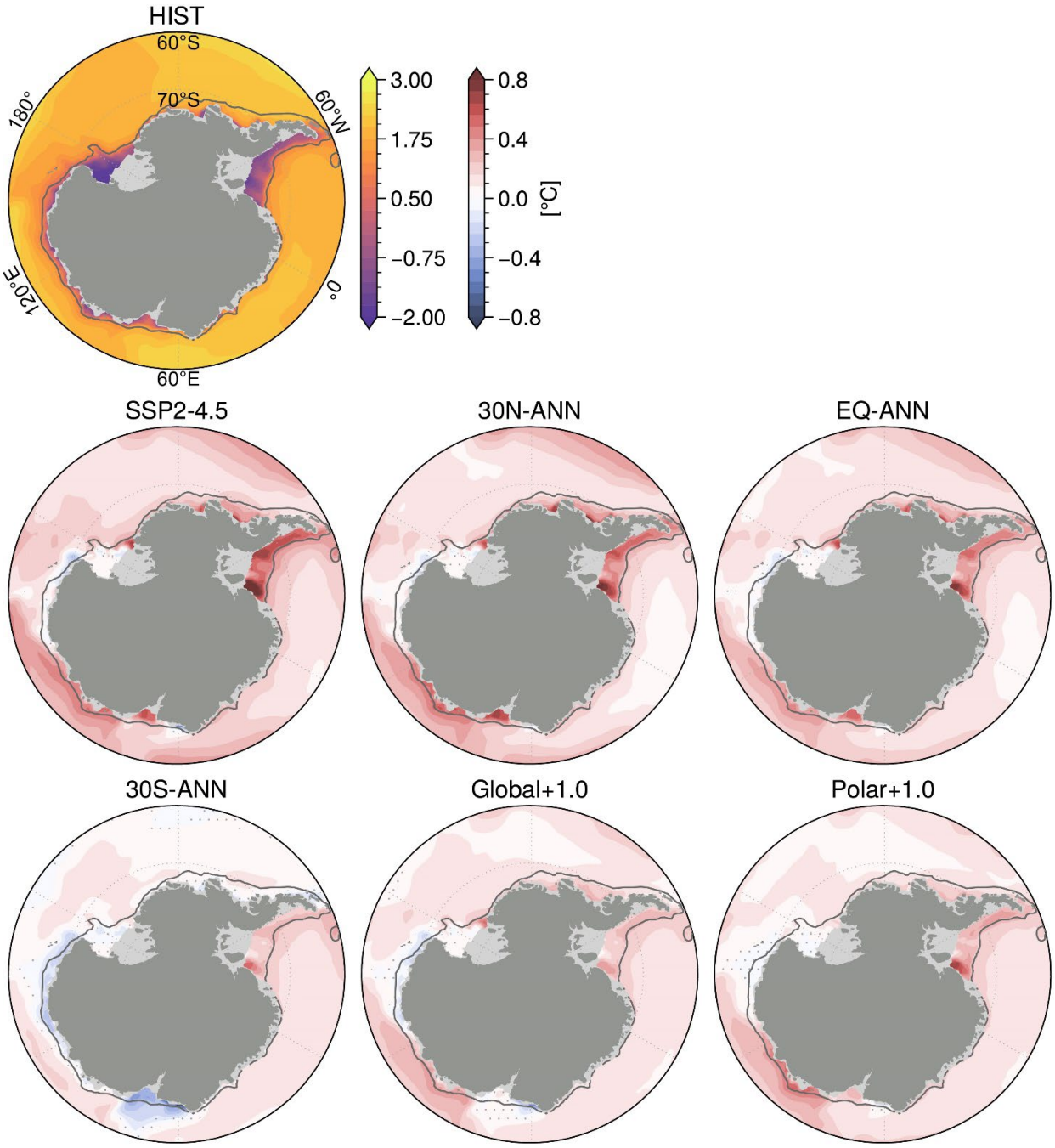

Figure 9. The top left panel shows the Historical annual ensemble mean (1990-2009) 100-1,000 m mean ocean potential temperature (°C). Shading in the following rows show the annual ensemble mean anomalies (2050-2069) from the Historical with respect to SSP2-4.5 and the SAI cases. Stippling shows the regions where the difference is not statistically significant. The dark gray contour follows the 1,500 m isobath.

To further analyze the drivers of subsurface shelf warming we now focus on regions where evidences of CDW (or modified CDW) have been observed: near the ice shelves in the Amundsen Sea (Jacobs et al., 1996), the Bellingshausen Sea (Jenkins and Jacobs, 2008), and

around East Antarctica near the Totten Glacier (~116°E) (Greenbaum et al., 2015), Vincennes Bay (~110°E) (Ribeiro et al., 2021), and Prydz Bay (~74°E) (Herraiz-Borreguero et al., 2015). To do so, we create a depth profile above the shelf and landward of the shelf break of vertical temperature advection averaged across the Amundsen-Bellingshausen Seas (ASBS) from 75°W – 130°W and in East Antarctica (EAIS) from 5°E – 140°E (see Figure 1 for these shelf boundary locations). Furthermore, we analyze cross-shelf transects of potential temperature, salinity, and potential density that are representative of these regions at 106°W (Amundsen Sea embayment) and at 74°E (Prydz Bay, see Figure 1 for these transect locations).

Focusing first on vertical temperature advection below ~150 m in the ASBS sector, 30N-ANN relative to the Historical shows an anomalous upward temperature advection at these depths (Figure 10, top right panel – dark gray line). These depths coincide with the largest temperature increases shown in a cross-shelf transect through the Amundsen Sea embayment (Figure 11). Figure 10 also shows the relative contribution to the change in vertical temperature advection ($\Delta(-w \times dT/dz)$) due to changes to the vertical velocity ($-\Delta w \times d\overline{T}/dz$), to the vertical temperature gradient ($-\overline{w} \times d\Delta T/dz$), and to the interaction between these perturbations ($-\Delta w \times d\Delta T/dz$), where the overbar denotes the Historical mean. Therefore, the second row in Figure 10 for 30N-ANN relative to the Historical shows that the anomalous upward vertical temperature advection below ~150 m is primarily driven by the combination of the decrease in downward vertical velocity and a decrease in the temperature gradient (a reduction in the temperature increase as depth increases – which represents a shoaling of the isotherms at these depths). These results are similar for the EQ-ANN anomalies (gray line) and the 15N-ANN anomalies (Figure S9 and S10).

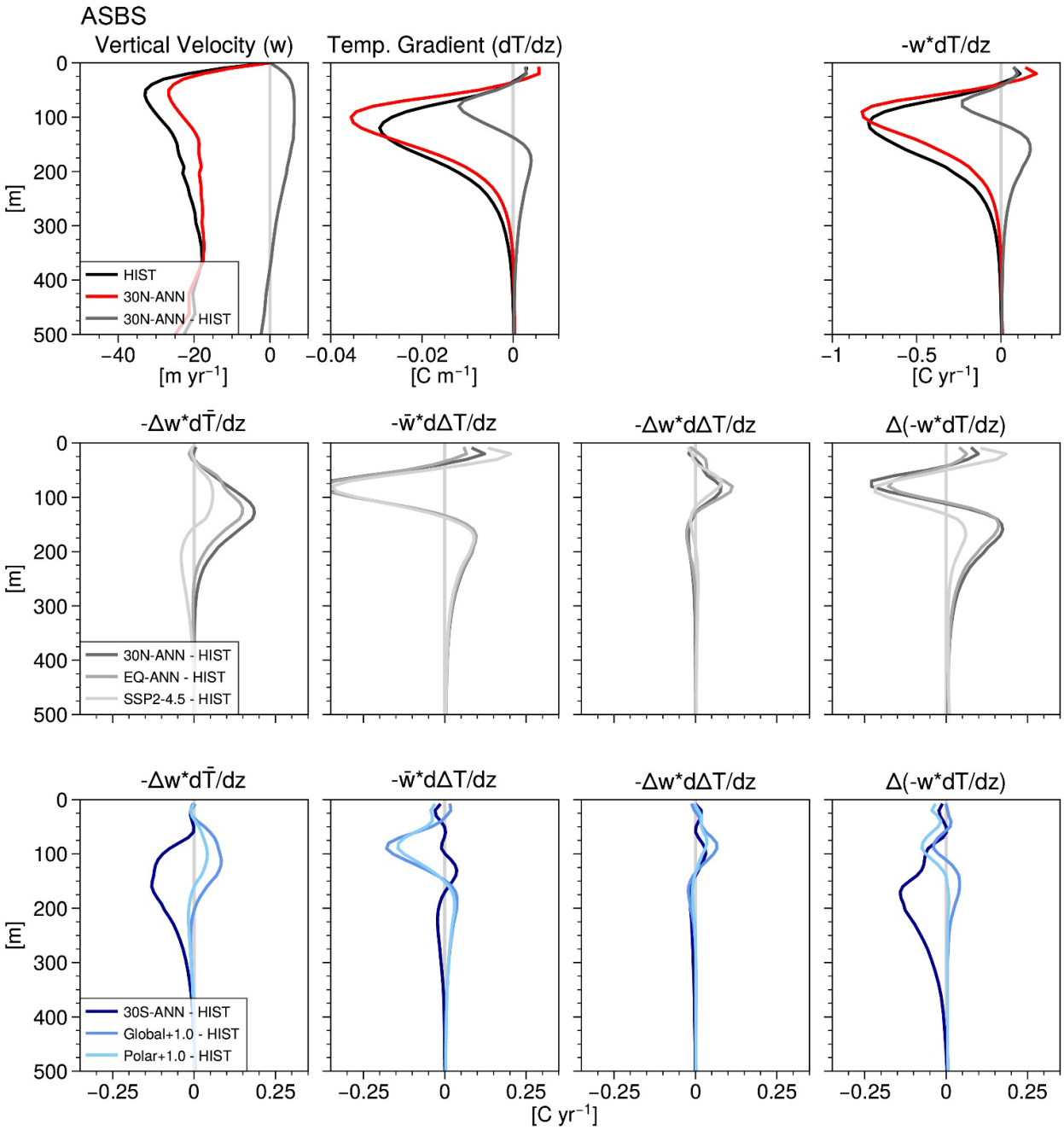

Figure 10. Vertical temperature advection and contributions to its change above the shelf in the ASBS sector. The top row shows Historical and 30N-ANN vertical velocity (m yr^{-1}), vertical temperature gradient (where negative values represent increasing temperature with increasing depth, °C m^{-1}), and vertical temperature advection (where the negative values represent a downward advection of colder surface water, °C yr^{-1}). The second and third row show the change in vertical temperature advection (far right column, $\Delta(-w \times dT/dz)$) and the contributions to this term due to the change in vertical velocity ($-\Delta w \times d\overline{T}/dz$), in the vertical temperature gradient ($-\overline{w} \times d\Delta T/dz$), and in the interaction between these perturbations ($-\Delta w \times d\Delta T/dz$), where the overbar denotes the Historical mean.

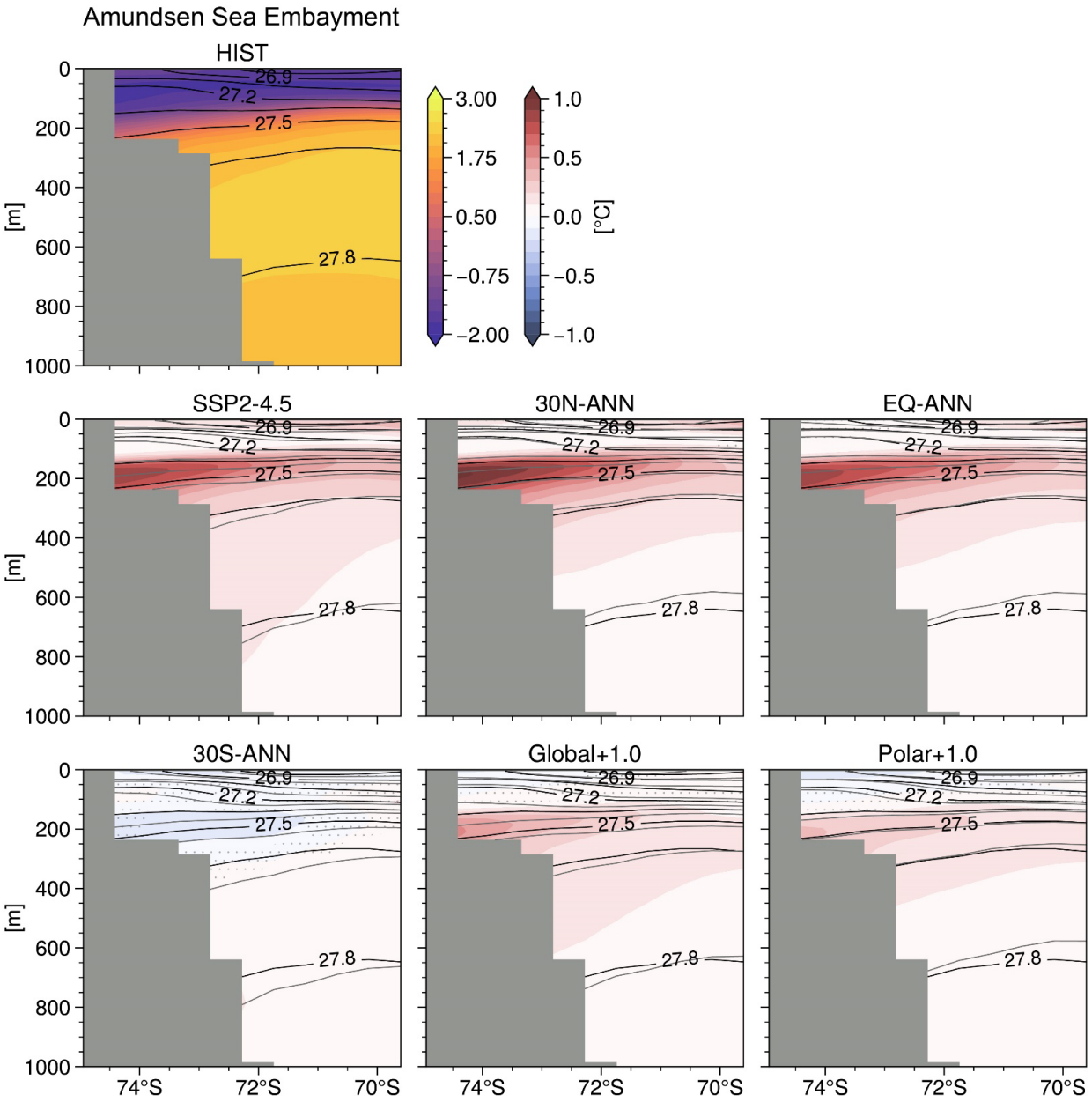

Figure 11. The top left panel shows the Amundsen Sea embayment cross-shelf transect at 106°W of potential temperature referenced to the surface (°C) with contours of constant potential density (isopycnals, minus 1,000 kg m^{-3}) for the Historical ensemble mean (1990-2009). Shading in the following rows show the annual ensemble mean temperature anomalies (2050-2069) from the Historical with respect to SSP2-4.5 and the SAI cases where stippling shows the regions where the difference is not statistically significant. In the difference panels, black contours mark the Historical isopycnals and gray contours mark the perturbed isopycnals (the lowest perturbed isopycnal is also 27.8 kg m^{-3}).

Furthermore, the upward temperature advection anomalies from below ~150 m for the 30N-ANN and EQ-ANN SAI cases are greater than for SSP2-4.5 (Figure 10, light gray line – middle row). In SSP2-4.5, the contribution of anomalous upward velocity to anomalous upward temperature advection below ~150 m is of the opposite magnitude compared to 30N-ANN and

EQ-ANN (middle row – first panel). This strengthening of the downward vertical velocity at depth in SSP2-4.5 may be explained by the greater surface freshwater flux relative to these SAI cases. The freshwater flux enhances vertical stratification and prevents upward advection of CDW. The role of freshwater forcing on 100-1000 m mean shelf temperature will be explained further below. Nonetheless, anomalous upward temperature advection persists below ~150 m in SSP2-4.5 due to the shoaling of CDW and the isotherms.

The anomalous warming below ~150 m for Global+1.0 and Polar+1.0 shown in the cross-shelf transect through the Amundsen Sea embayment (Figure 11) is also associated with a slight shoaling of the isotherms and reduction in the downward vertical velocity as shown in the ASBS sector (Figure 10 – bottom row). However, in the EAIS sector, Polar+1.0 shows greater anomalous upward temperature advection and larger shelf ocean temperature anomalies below ~150 m than Global+1.0 (Figures 12 and 13). This is due, at least in part, to slightly larger Ekman upwelling anomalies in the EAIS sector in Polar+1.0 (Figure 8) stemming from a more pronounced expression of a positive SAM phase and the associated weakening of the coastal easterly wind stress as compared to Global+1.0 (Figure 4). Another contributing factor to the enhanced upward temperature advection in Polar+1.0 relative to Global+1.0 may be associated with the larger shelf freshening and greater stratification in Global+1.0 which minimizes upward vertical velocity anomalies at these depths.

Analyzing the vertical temperature advection in the EAIS sector provides more insight to the role of freshwater forcing on 100-1000 m mean shelf temperature. The first panel in the middle row of Figure 12 (light gray line) shows that between ~50-400 m there is a suppression of the upward temperature advection due to changes in the vertical velocities leading to warming at these depths in SSP2-4.5 as compared to the Historical (Figure 13). This response is opposite to the expected increase in upward temperature advection due to the anomalous Ekman upwelling in this region (Figure 8). However, a significant surface freshwater flux driven by increases in iceberg calving and runoff in response to the ice accumulation gain and SAT increase above the nearby land in the EAIS sector (Figures 5 and 7) greatly stratifies the shelf water column preventing upward vertical velocity anomalies at these depths. This SSP2-4.5 freshening is shown in the 0-100 m mean salinity anomaly maps (Figures 14 and S11), in the deepening of the isopycnals above ~400 m (despite weaker Ekman downwelling), and in the salinity anomalies in the cross-shelf transect in Prydz Bay near the Amery Ice Shelf (Figures 15 and S12). This

stratification is shown to restrict the positive temperature anomalies to depths below ~200 m in the Prydz Bay cross-shelf transect (Figures 13 and S13).

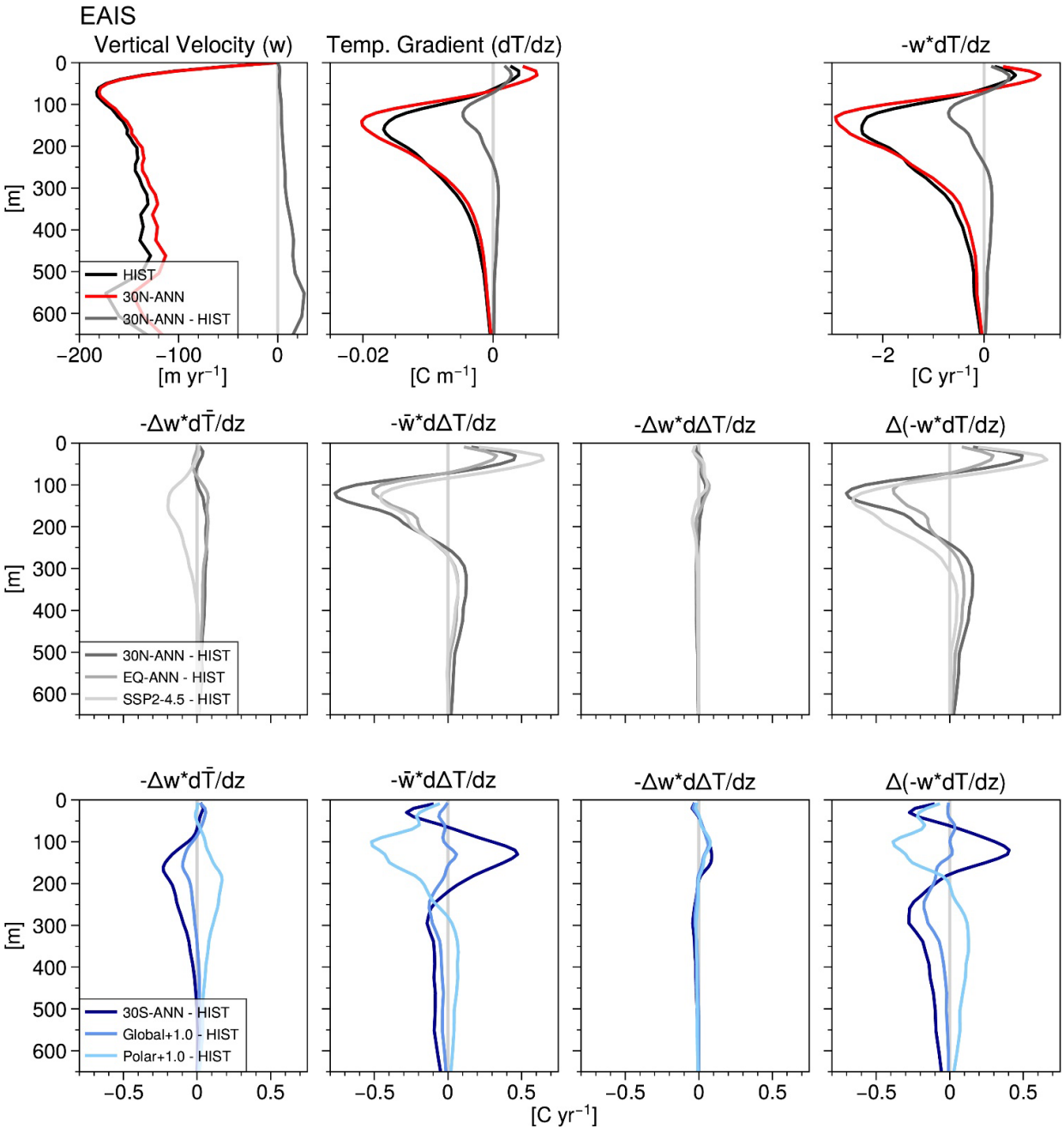

Figure 12. Same caption as for Figure 10 but showing the EAIS sector.

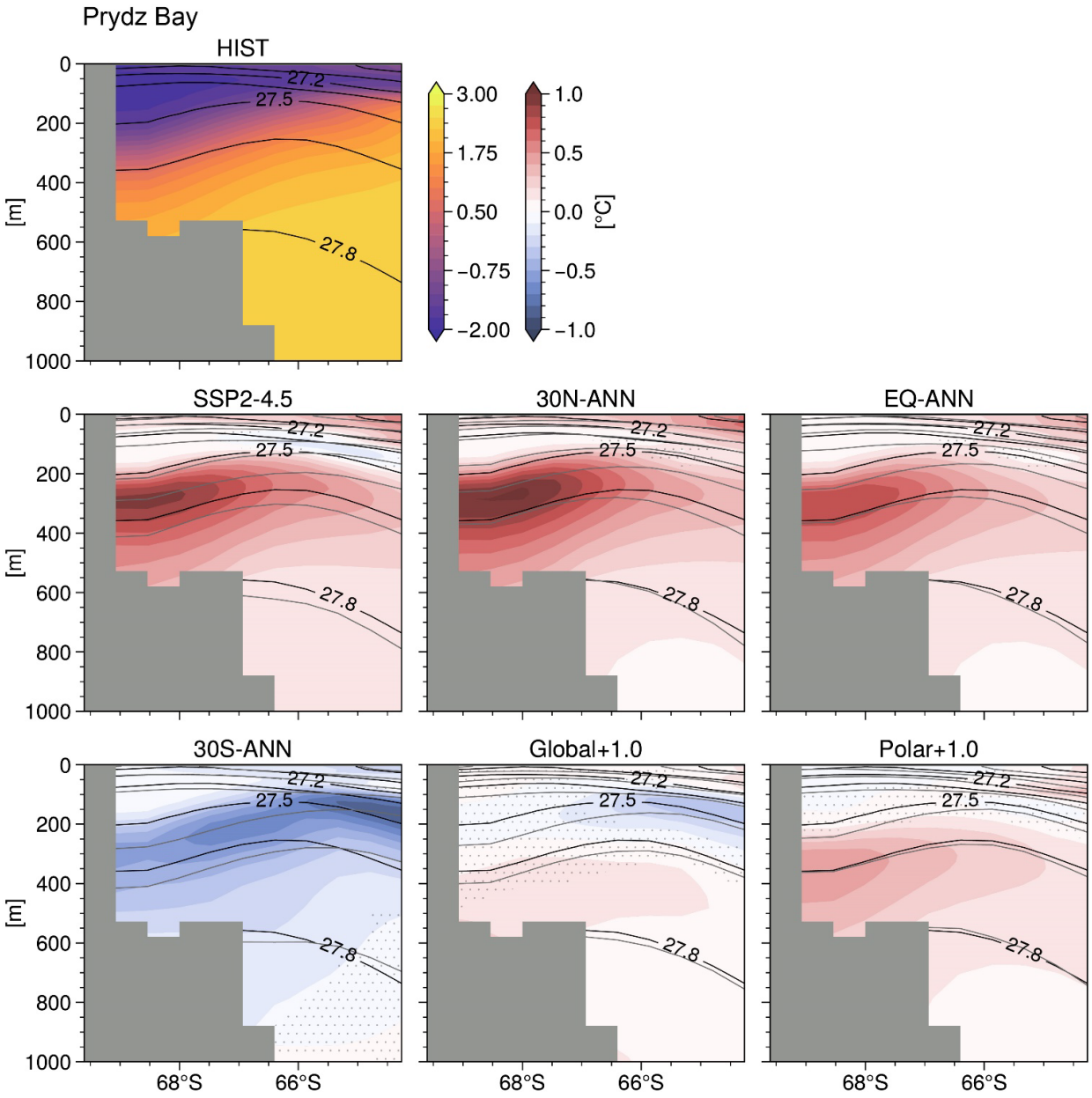

Figure 13. Same caption as for Figure 11 but showing the Prydz Bay cross-shelf transect at 74°E.

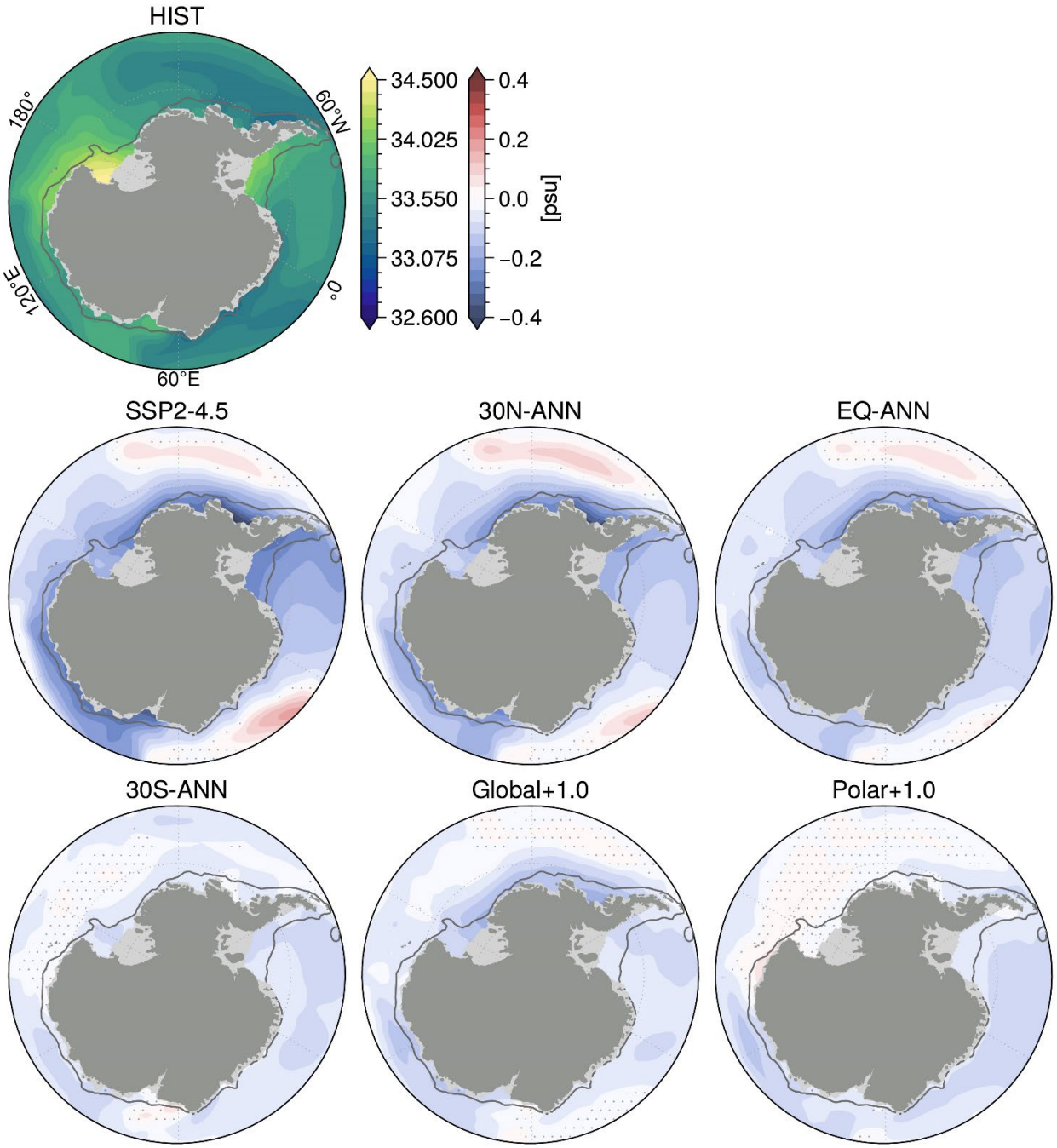

Figure 14. The top left panel shows the Historical annual ensemble mean (1990-2009) 0-100 m mean salinity (psu). Shading in the following rows show the annual ensemble mean anomalies (2050-2069) from the Historical with respect to SSP2-4.5 and the SAI cases. Stippling shows the regions where the difference is not statistically significant. The dark gray contour follows the 1,500 m isobath.

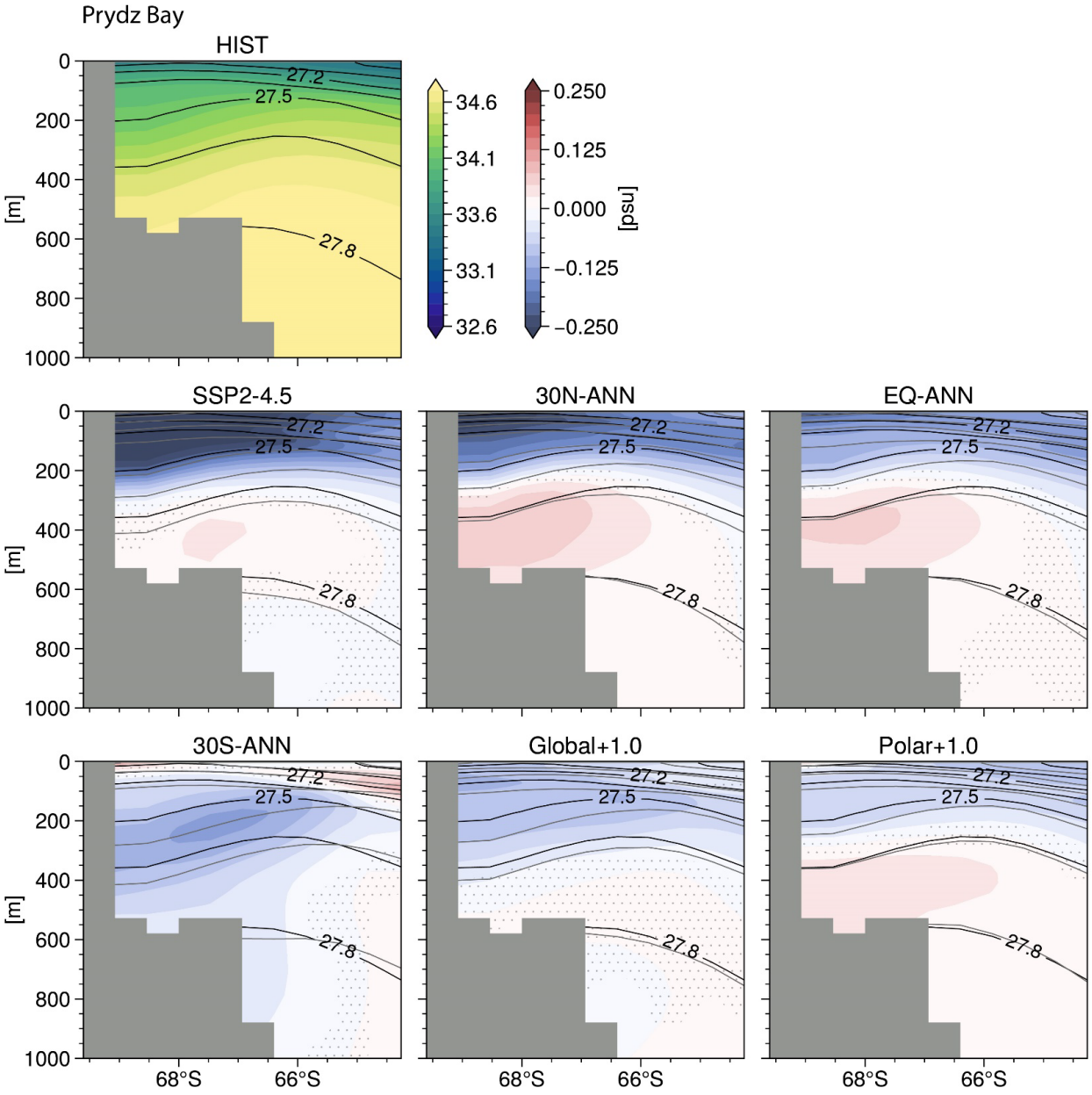

Figure 15. The top left panel shows the Prydz Bay cross-shelf transect at 74°E of salinity (psu) with contours of constant potential density (isopycnals, minus 1,000 kg m^{-3}) for the Historical ensemble mean (1990-2009). Shading in the following rows show the annual ensemble mean temperature anomalies (2050-2069) from the Historical with respect to SSP2-4.5 and the SAI cases where stippling shows the regions where the difference is not statistically significant. In the difference panels, black contours mark the Historical isopycnals and gray contours mark the perturbed isopycnals (the lowest perturbed isopycnal is also 27.8 kg m^{-3}).

Compared to SSP2-4.5, the smaller freshening anomalies and smaller changes to the isopycnal depth above ~400 m in 30N-ANN and EQ-ANN in the EAIS sector suggest that the vertical stratification does not inhibit upward temperature advection anomalies due to changes in vertical velocities as much. This result is illustrated by the positive values in Figure 12 (middle

599 row – left column). Therefore, in the Antarctic shelf ocean, vertical temperature advection
600 anomalies due to the changes to the vertical velocity term is a function of both changes to surface
601 wind stress and surface freshwater forcing. This conclusion is supported by previous research
602 which detail the relative contributions of freshwater forcing and wind stress changes to shelf
603 ocean warming (e.g., Goddard et al., 2017; Bronselaer et al., 2018, Beadling et al., 2022).
604 Finally, a cross-shelf transect of ocean salinity in the Amundsen Sea embayment is shown in
605 Figures 16 and S14 to aid with the analysis of the vertical temperature advection in Figures 10
606 and S9, and Figure S15 shows vertical temperature advection in the EAIS sector for the SAI
607 cases not included in main Figure 12.

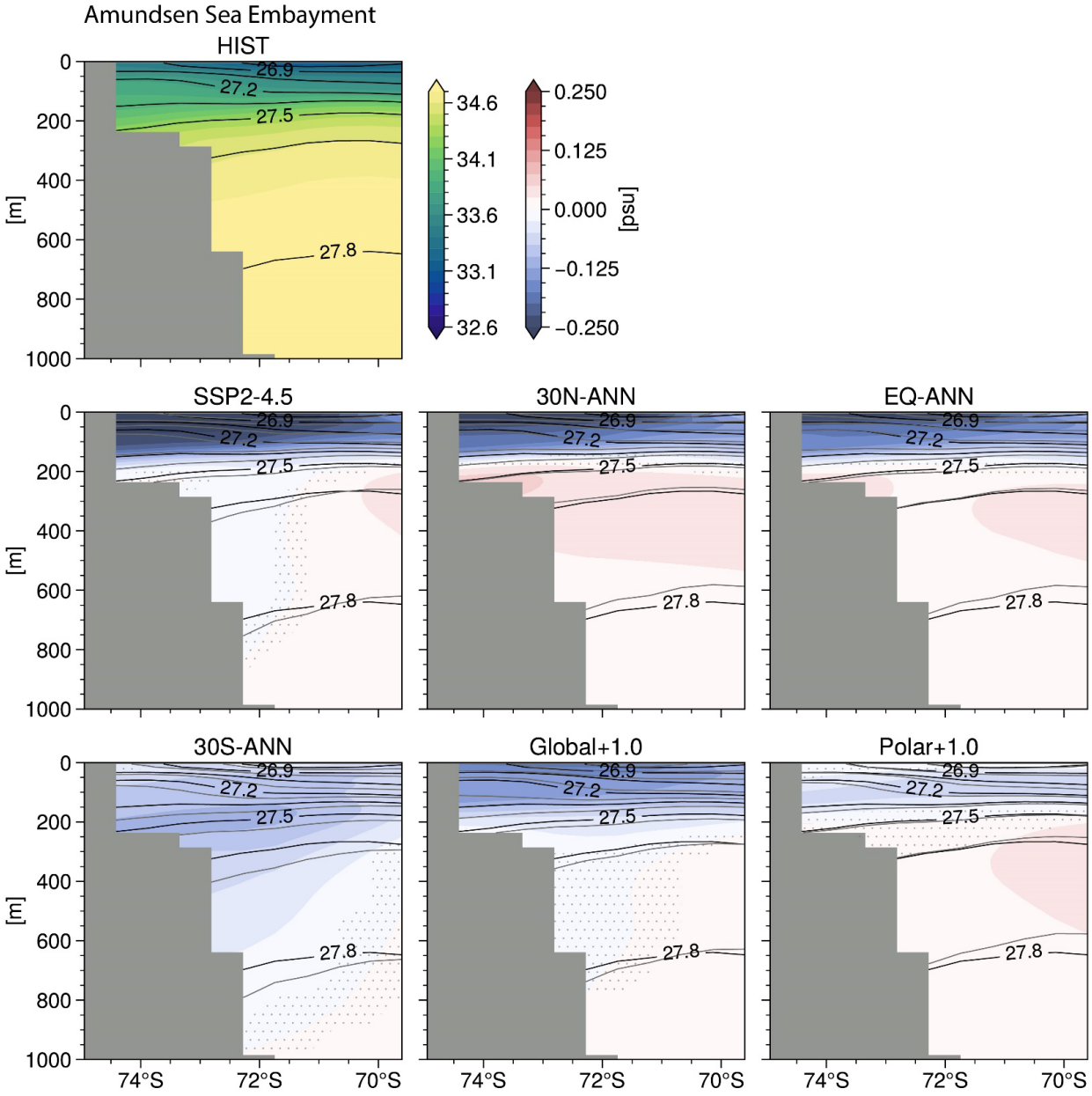

Figure 16. Same caption as for Figure 15 but showing the Amundsen Sea embayment cross-shelf transect at 106°W.

In summary, Antarctic shelf ocean warming below 100 m is initiated by changes to the surface wind stress and transferred to the ocean via Ekman upwelling anomalies. For the Equator and the NH single-latitude SAI cases, these Ekman upwelling anomalies bring warm CDW onto the continental shelf and increase shelf temperatures at depths pertinent to ice shelf basal melt. Conversely, the SH single-latitude SAI cases enhance Ekman downwelling, slow onshore CDW transport, and decrease 100-1000 m shelf temperature relative to the Historical. Both Global+1.0 and Polar+1.0 show less subsurface warming than SSP2-4.5 but vary among each other

(particularly in the shelf ocean near the EAIS) due to regional differences in surface wind stress and freshwater flux anomalies. Finally, in agreement with previous studies, results shown here suggest that upward temperature advection may be limited by enhanced ocean stratification due to surface freshening.

4 Discussion

Armstrong McKay et al. (2022) synthesize a multitude of studies to quantify the vulnerability of the Antarctic Ice Sheet and other climate tipping points with respect to future greenhouse gas warming. The authors identify that the global mean surface temperature threshold pertaining to the eventual collapse of the West Antarctic Ice Sheet is 1.5°C (min. 1.0°, max. 3.0°C) above the pre-industrial time period and that a 3.0°C (min. 2.0°, max. 6.0°C) temperature threshold is applicable to the eventual collapse of multiple subglacial basins in East Antarctica. Following the SSP2-4.5 emissions pathway entails that global mean temperature will reach the 1.5°C threshold in the early 2030s (Diffenbaugh and Barnes, 2023) and that temperatures will be nearly 3.0°C above the pre-industrial by the end of the 21st century (Meinshausen et al., 2020). If temperatures are maintained at 1.5°C or 3.0°C above the pre-industrial, the global mean sea level rise contribution from Antarctica is estimated to be about 1.0 (0.6-1.2) or 1.5 (1.0-2.0) meters by 2300, respectively; in comparison, the contribution is estimated to be about 9.6 (6.9-13.6, 17th-83rd percentiles) meters by 2300 if greenhouse gas emissions continue in the future along the business-as-usual RCP8.5 scenario (DeConto et al., 2021). Therefore, stratospheric aerosol injection has continued to be studied as a means of minimizing such risks and adverse impacts from exceeding these critical climate thresholds, at least until renewable energy implementation and/or carbon dioxide removal technologies are scaled globally.

4.1 Multi-latitude SAI cases compared to the 21st century SSP2-4.5 pathway

Relevant to the Antarctic Ice Sheet climate tipping points, the discussion below details whether the four multi-latitude SAI cases (Global+1.5, Global+1.0, Global+0.5, and Polar+1.0) will slow future 21st century Antarctic ice loss relative to years 2020-2039 and/or 2050-2069 in the SSP2-4.5 simulation when global mean temperature (GMT) is 1.5°C and 2.4°C above the pre-industrial level, respectively. We qualitatively determine whether ice loss is slowed by evaluating changes to surface ice accumulation and subsurface shelf ocean temperatures.

However, we note that coupled ice sheet simulations would be necessary to quantify the relative change in ice mass.

For this assessment, Figure 17 shows the annual ensemble mean area integrated ice accumulation (middle row) and the 100-1000 m mean shelf ocean temperature (bottom row) with respect to the Historical time period (1990-2009) for the WAIS, EAIS, or entire continent (columns) for each of the multi-latitude SAI cases, SSP2-4.5 (2020-2039), and SSP2-4.5 (2050-2069) relative to the GMT change from the pre-industrial for each ensemble mean (independent axis). This figure illustrates whether these SAI cases overcompensate (yellow shaded region) or undercompensate (green shaded region) these scalar metrics relative to the GMT change from the Historical-to-SSP2-4.5 pathway. The spatial response of the ice accumulation and subsurface shelf ocean temperature for these SAI cases with respect to SSP2-4.5 (2020-2039) and SSP2-4.5 (2050-2069) are shown in Figures S16 and S17.

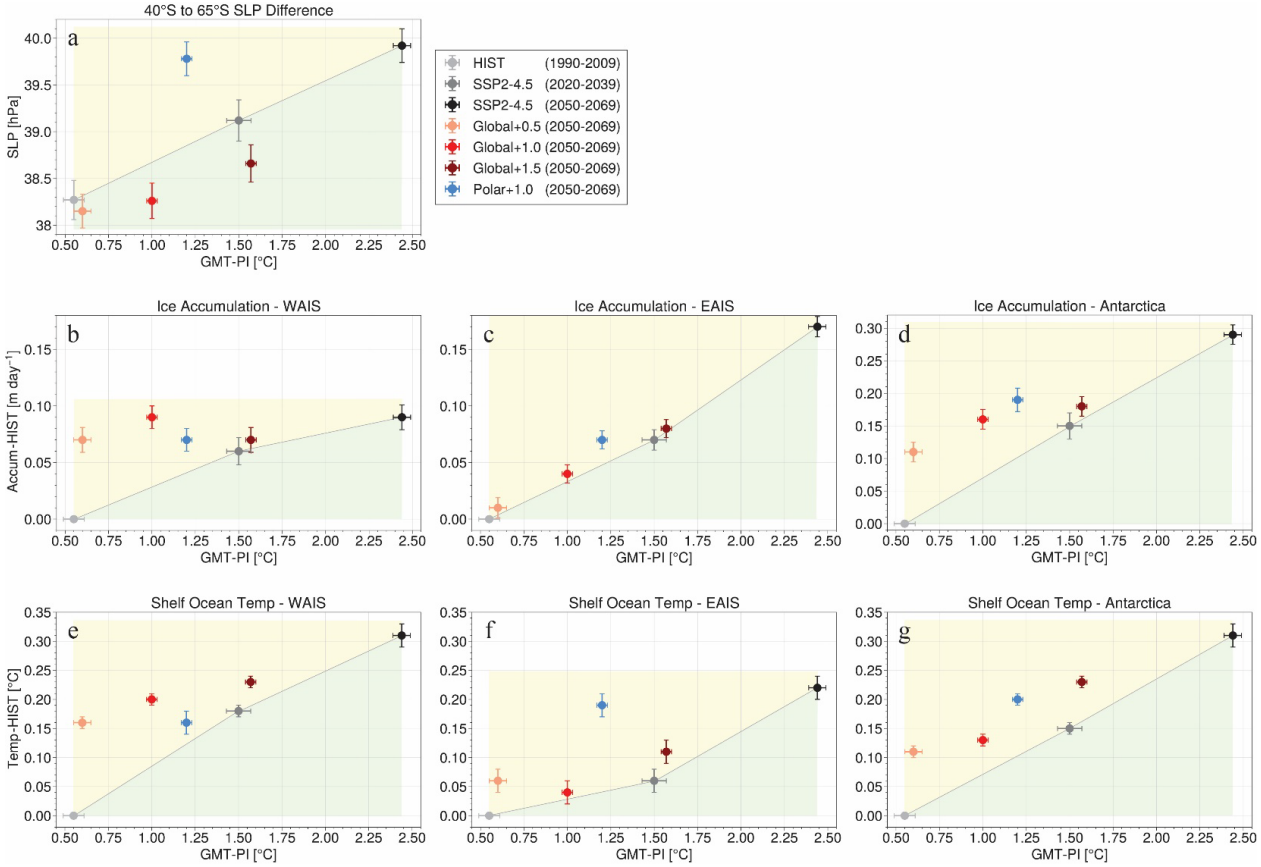

Figure 17. Scalar metrics versus the global mean temperature (GMT) change from the pre-industrial (independent axis) for the Historical, SSP2-4.5, and multi-latitude SAI cases. The top-left panel (a) shows the zonal mean sea level pressure difference from 40°S to 65°S. The middle row shows the integrated surface ice accumulation (m day^{-1}, with respect to the Historical) across the WAIS (from about 145˚W to 80˚W), EAIS (from about 15˚W to 163˚E), and the whole continent. The bottom row shows 100-1000 m

mean shelf ocean temperature (°C, with respect to the Historical) across the WAIS, EAIS, and whole continental shelf. All values represent the ensemble mean for years listed in the legend. The yellow and green shaded regions represent an overcompensation or undercompensation by the SAI case relative to the Historical-to-SSP2-4.5 pathway (the gray line segments connecting the Historical, SSP2-4.5 (2020-2039), and SSP2-4.5 (2050-2069) circles). The error bars represent plus-minus 1 standard error.

Figure 17 also shows in top left panel (a) the sea level pressure difference between 40°S and 65°S which represents the strength of the Southern Annular Mode (Gong and Wang, 1999, Marshall, 2003) relative to the GMT change for each of the simulation ensembles. Along the Historical-to-SSP2-4.5 pathway the SLP difference increases with increasing GMT – this highlights the projected 21st century positive SAM trend (Zheng et al., 2013; Coburn and Pryor, 2023). This panel also illustrates that Polar+1.0 will result in a more robust positive SAM pattern than is projected along the Historical-to-SSP2-4.5 pathway; and shows that for all the Global+ cases the SLP difference represents a negative SAM pattern relative to the Historical-to-SSP2-4.5 pathway. This relative overcompensation in Polar+1.0 and undercompensation in the Global+ cases is consistent with the SLP and surface wind stress anomaly patterns shown in Figures 3 and S2 and critically influences ice accumulation and shelf ocean temperature patterns as examined in the Results section.

Regarding mass changes to the WAIS, Figure 17b shows that there is an overcompensation of ice accumulation per unit increase in GMT in the multi-latitude SAI cases relative to the Historical-to-SSP2-4.5 pathway. Notably, for each of these SAI cases WAIS ice accumulation will be greater than the SSP2-4.5 2020-2039 mean accumulation. This increase signifies that all of the multi-latitude SAI cases will accumulate more WAIS ice at the surface through precipitation as compared to the SSP2-4.5 time period when its temperature tipping point is reached (1.5°C, 2020-2039). Nonetheless, this increase in ice accumulation is likely to play a secondary role in the change to the overall WAIS mass balance as previous research shows that the WAIS projected mass change will be dominated by ice shelf basal melt due to ocean thermal forcing (Chambers et al., 2022; Siahaan et al., 2022).

Figure 17e shows that there would be an overcompensation of the mean subsurface shelf ocean temperature near the WAIS in these SAI cases, indicating that the regional ocean is warmer per unit increase in GMT than along the Historical-to-SSP2-4.5 pathway. Markedly, the Global+1.5 (dark red circle) and Global+1.0 (red circle) cases result in warmer shelf ocean temperatures near the WAIS as compared to SSP2-4.5 (2020-2039) when the GMT is 1.5°C

above the pre-industrial (gray circle). Of the multi-latitude injection cases considered in this study only the Polar+1.0 and Global+0.5 cases keep shelf ocean temperatures below SSP2-4.5 (2020-2039) which represents the climate tipping point temperature threshold for the self-perpetuating, eventual collapse of the WAIS (Armstrong McKay et al., 2022). Therefore, to hold shelf ocean temperatures near the WAIS below this threshold through the mid-to-late 21st century (2050-2069), one would have to cool GMT by 1°C if considering a multi-latitude injection at low latitudes (Global+0.5) or by 0.5°C if considering a high-latitude injection case (Polar+1.0). That said, it is important to note that all multi-latitude SAI cases considered here keep shelf ocean temperatures near the WAIS significantly below the mean value of SSP2-4.5 during 2050-2069 (black circle).

Regarding the EAIS, previous observations show the presence of CDW (or modified CDW) on the shelf and increased basal melt rates at locations between Prydz Bay and the Ross Sea (Figure 1) (e.g., Greenbaum et al., 2015; Rignot et al., 2019; Smith et al., 2020). This area includes two subglacial basins near the George V Land and Wilkes Land that are vulnerable to rapid melting if the warm CDW reaches the regional ice shelves (Herraiz-Borreguero and Naveira Garabato, 2022; Iizuka et al., 2023). Armstrong McKay et al. (2022) estimate that for these East Antarctic subglacial basins the GMT above the pre-industrial threshold is 3.0°C, with a minimum threshold of 2.0°. Therefore, to minimize the risk of EAIS collapse, we now discuss each multi-latitude SAI case relative to the SSP2-4.5 pathway when GMT is at least 2.0°C above the pre-industrial.

Figure 17f shows the mean subsurface shelf ocean temperature change near the EAIS (relative to the Historical) per unit increase in GMT for the multi-latitude SAI cases and the Historical-to-SSP2-4.5 pathway. Although the three Global+ cases warm the regional shelf ocean more than the Historical-to-SSP2-4.5 pathway (an overcompensation), all temperatures are significantly lower than the mean shelf temperature increase (~0.15°C) associated with a +2.0°C GMT increase and the low-end temperature threshold for the EAIS subglacial basins climate tipping point (Armstrong McKay et al., 2022). Conversely, the EAIS shelf warming in the Polar+1.0 strategy (blue circle) is greater than the low-end temperature threshold and is not statistically different from the SSP2-4.5 2050-2069 mean (black circle) wherein GMT is about 2.4°C above the pre-industrial. This EAIS shelf warming result in Polar+1.0 is driven by the positive SAM response, weakening coastal easterlies, and increased CDW upwelling shown in

729 the Results section. Furthermore, the Polar+1.0 surface ice accumulation overcompensation
730 (Figure 17c) is far less than the shelf ocean warming overcompensation which implies that the
731 EAIS mass loss under this SAI case would be more similar to the mid-to-late century SSP2-4.5
732 pathway than a pathway that uses a Global+ injection strategy.

733 Integrating these results across all of Antarctica, we highlight here that the Global+0.5 or
734 Global+1.0 SAI cases show distinct benefits concerning ice mass balance as compared to the
735 Global+1.5 or Polar+1.0 cases as well as to the SSP2-4.5 pathway with no SAI. Figure 17d
736 shows that relative to the Historical-to-SSP2-4.5 pathway, Global+0.5 and Global+1.0
737 overcompensate Antarctic surface ice accumulation as much or more than the Global+1.5 or
738 Polar+1.0 SAI cases relative to the Historical-to-SSP2-4.5 pathway. Therefore, atmospheric
739 circulation changes induced by Global+0.5 and Global+1.0 (namely the onshore winds near the
740 WAIS due to the developed Pacific-South America pattern, Figures 3 and S2) bring more snow
741 and ice accumulation to the Antarctic continent relative to the change in GMT and relative to
742 Global+1.5 or Polar+1.0 (as well as the Historical-to-SSP2-4.5 pathway). Furthermore, in both
743 Polar+1.0 and Global+1.5 the mean Antarctic shelf ocean temperature is significantly warmer
744 due to associated changes in CDW upwelling as compared to Global+0.5 and Global+1.0.
745 Finally, despite similar integrated ice accumulation and mean shelf ocean temperature across
746 Antarctica, it is important to recall that Global+0.5 keeps the WAIS shelf ocean below the 1.5°C
747 temperature threshold, while Global+1.0 exceeds this threshold and may result in passing the
748 WAIS tipping point. Therefore, for our simulations utilizing SAI to cool GMT to 0.5°C above
749 the pre-industrial, as represented by the Global+0.5 case, would be needed to minimize this risk.

750 **4.2 Limitations and future work**

751 While the high-latitude SH atmospheric response to various SAI cases shown in this
752 study is consistent with previous SAI studies (McCusker et al., 2015; Bednarz et al., 2022), the
753 role SAI can play in the Antarctic region has generally not yet been extensively studied and as
754 such remains relatively poorly understood. The detailed evaluation of the Antarctic shelf ocean
755 response to multiple SAI cases has not, to our knowledge, been performed before and as such our
756 work constitutes a novel contribution to this research field for which direct comparisons to
757 previous SAI research are not applicable. It is therefore important to discuss the relevant
758 limitations of the model and concerns regarding its representation of the shelf ocean physics.

One key limitation is the relatively weak lateral density gradient associated with the Antarctic Slope Front (ASF) in these simulations as compared to observations (e.g., the World Ocean Circulation Experiment, Sparrow et al. (2011)) and other studies which examine cross-ASF heat transport using higher resolved ocean models (e.g., Goddard et al., 2017; Stewart et al., 2018; Palóczy et al., 2018). The weak ASF is characterized by flatter isopycnals near the shelf break (see contours in Figures 11 and 13) which create additional pathways for along-isopycnal onshore transport of CDW as compared to these previous studies and observations. Conversely, the horizontal ocean resolution in the current study (~1° at 70°S) is too coarse to resolve ocean eddies which are an important mechanism for onshore heat transport through the ASF (e.g., Goddard et al., 2017; Stewart et al., 2018; Palóczy et al., 2018).

Furthermore, previous studies show that the model representation of the ASF is critical to the effect that surface freshwater forcing has on CDW-induced shelf warming. Namely, in models with <0.25° horizontal resolution the shelf ocean surface freshening promotes a strengthening of the ASF which keeps the freshwater on the shelf, strengthens the ASF, and minimizes onshore cross-ASF heat transport (Goddard et al., 2017; Moorman et al., 2020; Beadling et al., 2022). Conversely, in coarser ocean models the surface freshening anomalies can extend away from the continental shelf and stratify the surface layers which flatten the isopycnals that would otherwise reach the surface and transport heat to the overlying atmosphere or sea ice. Instead, the heat is directed towards the shelf along the flattened isopycnals (Bronselaer et al., 2018; Golledge et al., 2019; Beadling et al., 2022). In the current study, the interaction between the ASF, surface freshening, and shelf warming are more aligned with the latter studies wherein a relatively weak ASF permits onshore heat transport at depth along relatively flat isopycnals. This heat is then maintained above the continental shelf due to surface freshening and the resultant vertical stratification which reduces upward vertical heat advection (see Figures 10-13). The relative role of increased melt flux into the shelf ocean and its effect on shelf temperatures remains an active area of research in the ocean modeling community.

Despite uncertainties regarding the impact of freshwater forcing and numerical limitations of the ocean model used in this study, the subsurface shelf ocean temperature response in SSP2-4.5 are consistent with previous studies which show a similar temperature response with respect to changes to the coastal easterlies (e.g., Spence et al., 2014; Goddard et al., 2017; Beadling et al., 2022). Additionally, the results here are consistent with Palóczy et al.

(2018) that shows shelf ocean warming during a positive phase SAM (weaker coastal easterlies) along the WAIS coastline and western Antarctic Peninsula coastline as well as in the eastern-EAIS region.

Additionally, it is important to consider model dependence on the simulated climate responses to SAI. Fasullo and Richter (2023) show that rapid climate adjustments to CO_2 forcing can vary significantly from model to model and thus the choice of the background emission scenario in an SAI simulation is vital to the simulated output. Furthermore, the control algorithm, which dictates the amount of injection at each latitude in the multi-latitude SAI cases to achieve certain climate objectives such as a GMT target, will likely inject SO_4 precursors at different amounts at different latitudes for different studies. In this study, the Global+ cases injected the majority of the SO_4 precursors in the southern hemisphere which led to atmospheric circulation changes more beneficial to Antarctic ice than the response if the major of the injection was in the northern hemisphere. Such nuances to simulation design are critical to consider as the SAI research community moves forward.

Moving forward, it would be beneficial to have a coupled Antarctic ice sheet to facilitate a quantitative mass balance analysis. This addition would improve the current assessment of Antarctic ice loss, which qualitatively assesses whether ice loss would decrease in the multi-latitude SAI cases by looking at relative changes to ice accumulation and shelf ocean temperature as compared to SSP2-4.5. Furthermore, Fasullo and Richter (2023) show that rapid climate adjustments to CO_2 forcing can vary significantly from model to model and thus the choice of the background emission scenario in an SAI simulation is vital to the simulated output. Therefore, a qualitative assessment of the impacts of varying SAI strategies on the Antarctic ice mass balance should be performed in a multi-model framework in order to narrow the uncertainty arising from model representation of various physical processes. Additionally, in this study the Global+ cases injected the majority of the SO_4 precursors in the southern hemisphere which led to atmospheric circulation changes more beneficial to Antarctic ice than the response if the major of the injection was in the northern hemisphere. Future work will build upon the Global+ SAI cases to see whether changes to the injection strategy, in a manner introduced in Zhang et al. (2023) and Bednarz et al. (2023), would further slow Antarctic mass loss.

5 Conclusions

This study uses seven different single-latitude stratospheric aerosol injection (SAI) cases and four different multi-latitude SAI cases to assess the resulting SAI impacts on the Antarctic climate, namely surface ice accumulation and subsurface shelf ocean temperature. These cases are compared to a historical time period (1990-2009) and to select time periods along the 21st century SSP2-4.5 emissions pathway that represent global mean temperature thresholds relevant to Antarctic ice sheet tipping points. Of the multi-latitude SAI cases, we find that the Global+0.5 or the Polar+1.0 case can maintain subsurface shelf ocean temperatures near the West Antarctic Ice Sheet (WAIS) below the temperature threshold that is estimated to initiate the eventual collapse of the ice sheet (Armstrong McKay et al., 2022). However, relative to three Global+(0.5, 1.0, 1.5) cases, the Polar+1.0 strategy significantly warms the shelf ocean near the East Antarctic Ice Sheet (EAIS) and results in ocean temperatures above the low-end estimate for the tipping point of subglacial basins in the EAIS (Armstrong McKay et al., 2022). This is due to the Polar+1.0 case initiating southern hemisphere sea level pressure and wind stress anomalies with respect to the Historical simulation analogous to patterns correlated with the positive phase of the Southern Annular Mode. Around East Antarctica in particular, this positive mode is associated with weaker coastal easterlies and more upwelling of warm Circumpolar Deep Water onto the continental shelf at depths pertinent to ice shelf basal melt. Therefore, for the multi-latitude SAI cases considered here, the Global+0.5 SAI strategy would minimize the most risk associated with the future melt and potential collapse of significant regions of the Antarctic Ice Sheet.

In summary, while some of the results could be model dependent, our CESM2(WACCM6) simulations demonstrate that the multi-latitude SAI cases considered here all slow Antarctic ice loss relative to the mid-to-late century SSP2-4.5 pathway, though using SAI to cool global mean temperatures to 0.5°C above the pre-industrial (the Global+0.5 case) may be necessary to avoid Antarctic ice sheet tipping points. These results highlight the complexity of factors driving the SAI-induced impacts on the Antarctic system and demonstrate the crucial role of the injection strategy in determining the effectiveness of SAI in preventing future losses of Antarctic ice.

Acknowledgments

This research was supported in part by Lilly Endowment, Inc., through its support for the Indiana University Pervasive Technology Institute. Support for BK was provided in part by the National Science Foundation through agreement SES-1754740, NOAA's Climate Program Office, Earth's Radiation Budget (ERB) (Grant NA22OAR4310479), and the Indiana University Environmental Resilience Institute. The Pacific Northwest National Laboratory is operated for the US Department of Energy by Battelle Memorial Institute under contract DE-AC05-76RL01830. We would like to acknowledge high-performance computing support from Cheyenne (https://doi.org/10.5065/D6RX99HX) provided by NCAR's Computational and Information Systems Laboratory, sponsored by the National Science Foundation. Support was also provided by the Atkinson Center for Sustainability at Cornell University, and by the National Science Foundation through agreement CBET-2038246. EMB also acknowledges support from the NOAA cooperative agreement NA22OAR4320151 and the NOAA Earth's Radiative Budget initiative.

Open Research

P.B. Goddard is currently creating a repository on Zenodo that will include all data and code to make the figures and tables in this manuscript.

References

Adusumilli, S., A. Fish, M., Fricker, H. A., & Medley, B. (2021). Atmospheric River Precipitation Contributed to Rapid Increases in Surface Height of the West Antarctic Ice Sheet in 2019. *Geophysical Research Letters*, *48*(5), e2020GL091076. https://doi.org/10.1029/2020GL091076

Alley, R. B., Anandakrishnan, S., Christianson, K., Horgan, H. J., Muto, A., Parizek, B. R., et al. (2015). Oceanic Forcing of Ice-Sheet Retreat: West Antarctica and More. *Https://Doi.Org/10.1146/Annurev-Earth-060614-105344*, *43*, 207–231. https://doi.org/10.1146/ANNUREV-EARTH-060614-105344

Bassis, J. N., Berg, B., Crawford, A. J., & Benn, D. I. (2021). Transition to marine ice cliff instability controlled by ice thickness gradients and velocity. *Science*, *372*(6548), 1342–1344. https://doi.org/10.1126/SCIENCE.ABF6271/SUPPL_FILE/ABF6271S5.MP4

Beadling, R. L., Krasting, J. P., Griffies, S. M., Hurlin, W. J., Bronselaer, B., Russell, J. L., et al. (2022). Importance of the Antarctic Slope Current in the Southern Ocean Response to Ice Sheet Melt and Wind Stress Change. *Journal of Geophysical Research: Oceans*, *127*(5). https://doi.org/10.1029/2021JC017608

Bednarz, E. M., Visioni, D., Richter, J. H., Butler, A. H., & MacMartin, D. G. (2022). Impact of the Latitude of Stratospheric Aerosol Injection on the Southern Annular Mode. *Geophysical Research Letters*, *49*(19), e2022GL100353. https://doi.org/10.1029/2022GL100353

Bednarz, E. M., Visioni, D., Kravitz, B., Jones, A., Haywood, J. M., Richter, J., et al. (2023). Climate response to off-equatorial stratospheric sulfur injections in three Earth system models – Part 2: Stratospheric and free-tropospheric response. *Atmospheric Chemistry and Physics*, *23*(1), 687–709. https://doi.org/10.5194/ACP-23-687-2023

Berdahl, M., Robock, A., Ji, D., Moore, J. C., Jones, A., Kravitz, B., & Watanabe, S. (2014). Arctic cryosphere response in the Geoengineering Model Intercomparison Project G3 and G4 scenarios. *Journal of Geophysical Research: Atmospheres*, *119*(3), 1308–1321. https://doi.org/10.1002/2013JD020627

Bronselaer, B., Winton, M., Griffies, S. M., Hurlin, W. J., Rodgers, K. B., Sergienko, O. V., et al. (2018). Change in future climate due to Antarctic meltwater. *Nature 2018 564:7734*, *564*(7734), 53–58. https://doi.org/10.1038/s41586-018-0712-z

Bull, C. Y. S., Jenkins, A., Jourdain, N. C., Vaňková, I., Holland, P. R., Mathiot, P., et al. (2021). Remote Control of Filchner-Ronne Ice Shelf Melt Rates by the Antarctic Slope Current. *Journal of Geophysical Research: Oceans*, *126*(2), e2020JC016550. https://doi.org/10.1029/2020JC016550

Chambers, C., Greve, R., Obase, T., Saito, F., & Abe-Ouchi, A. (2022). Mass loss of the Antarctic ice sheet until the year 3000 under a sustained late-21st-century climate. *Journal of Glaciology*, *68*(269), 605–617. https://doi.org/10.1017/JOG.2021.124

Clem, K. R., Renwick, J. A., & McGregor, J. (2017). Relationship between eastern tropical Pacific cooling and recent trends in the Southern Hemisphere zonal-mean circulation. *Climate Dynamics*, *49*(1–2), 113–129. https://doi.org/10.1007/S00382-016-3329-7/FIGURES/14

Coburn, J., & Pryor, S. C. (2022). Evolution of the Internal Climate Modes under Future Warming. *Journal of Climate*, *36*(2), 511–529. https://doi.org/10.1175/JCLI-D-22-0200.1

Daae, K., Hattermann, T., Darelius, E., Mueller, R. D., Naughten, K. A., Timmermann, R., & Hellmer, H. H. (2020). Necessary Conditions for Warm Inflow Toward the Filchner Ice Shelf, Weddell Sea. *Geophysical Research Letters*, *47*(22), e2020GL089237. https://doi.org/10.1029/2020GL089237

Dai, Z., Weisenstein, D. K., & Keith, D. W. (2018). Tailoring Meridional and Seasonal Radiative Forcing by Sulfate Aerosol Solar Geoengineering. *Geophysical Research Letters*, *45*(2), 1030–1039. https://doi.org/10.1002/2017GL076472

Danabasoglu, G., Lamarque, J. F., Bacmeister, J., Bailey, D. A., DuVivier, A. K., Edwards, J., et al. (2020). The Community Earth System Model Version 2 (CESM2). *Journal of Advances in Modeling Earth Systems*, *12*(2). https://doi.org/10.1029/2019MS001916

Danabasoglu, G., Bates, S. C., Briegleb, B. P., Jayne, S. R., Jochum, M., Large, W. G., et al. (2012). The CCSM4 Ocean Component. *Journal of Climate*, *25*(5), 1361–1389. https://doi.org/10.1175/JCLI-D-11-00091.1

Davis, N. A., Visioni, D., Garcia, R. R., Kinnison, D. E., Marsh, D. R., Mills, M. J., et al. (2022). Climate, variability, and climate sensitivity of "Middle Atmosphere" chemistry configurations of the Community Earth System Model Version 2, Whole Atmosphere Community Climate Model Version 6 (CESM2(WACCM6)). *Authorea Preprints*. https://doi.org/10.22541/ESSOAR.167117634.40175082/V1

Davison, B. J., Hogg, A. E., Rigby, R., Veldhuijsen, S., van Wessem, J. M., van den Broeke, M. R., et al. (2023). Sea level rise from West Antarctic mass loss significantly modified by large snowfall anomalies. *Nature Communications 2023 14:1*, *14*(1), 1–13. https://doi.org/10.1038/s41467-023-36990-3

DeConto, R. M., & Pollard, D. (2016). Contribution of Antarctica to past and future sea-level rise. *Nature*, *531*(7596), 591–597. https://doi.org/10.1038/nature17145

DeConto, R. M., Pollard, D., Alley, R. B., Velicogna, I., Gasson, E., Gomez, N., et al. (2021). The Paris Climate Agreement and future sea-level rise from Antarctica. *Nature 2021 593:7857*, *593*(7857), 83–89. https://doi.org/10.1038/s41586-021-03427-0

Diffenbaugh, N. S., & Barnes, E. A. (2023). Data-driven predictions of the time remaining until critical global warming thresholds are reached. *Proceedings of the National Academy of Sciences of the United States of America*, *120*(6), e2207183120. https://doi.org/10.1073/PNAS.2207183120/SUPPL_FILE/PNAS.2207183120.SAPP.PDF

Ding, Q., Steig, E. J., Battisti, D. S., & Küttel, M. (2011). Winter warming in West Antarctica caused by central tropical Pacific warming. *Nature Geoscience 2011 4:6*, *4*(6), 398–403. https://doi.org/10.1038/ngeo1129

Dinniman, M. S., Klinck, J. M., & Smith, W. O. (2011). A model study of Circumpolar Deep Water on the West Antarctic Peninsula and Ross Sea continental shelves. *Deep Sea Research Part II: Topical Studies in Oceanography*, *58*(13–16), 1508–1523. https://doi.org/10.1016/J.DSR2.2010.11.013

Donat-Magnin, M., Jourdain, N. C., Spence, P., Le Sommer, J., Gallée, H., & Durand, G. (2017). Ice-Shelf Melt Response to Changing Winds and Glacier Dynamics in the Amundsen Sea Sector, Antarctica. *Journal of Geophysical Research: Oceans*, *122*(12), 10206–10224. https://doi.org/10.1002/2017JC013059

Dotto, T. S., Naveira Garabato, A. C., Wåhlin, A. K., Bacon, S., Holland, P. R., Kimura, S., et al. (2020). Control of the Oceanic Heat Content of the Getz-Dotson Trough, Antarctica, by the Amundsen Sea Low. *Journal of Geophysical Research: Oceans*, *125*(8), e2020JC016113. https://doi.org/10.1029/2020JC016113

Espinoza, V., Waliser, D. E., Guan, B., Lavers, D. A., & Ralph, F. M. (2018). Global Analysis of Climate Change Projection Effects on Atmospheric Rivers. *Geophysical Research Letters*, *45*(9), 4299–4308. https://doi.org/10.1029/2017GL076968

Fasullo, J. T., & Richter, J. H. (2023). Dependence of strategic solar climate intervention on

961 background scenario and model physics. *Atmospheric Chemistry and Physics*, *23*(1), 163–
962 182. https://doi.org/10.5194/ACP-23-163-2023

963 Gettelman, A., Mills, M. J., Kinnison, D. E., Garcia, R. R., Smith, A. K., Marsh, D. R., et al.
964 (2019). The Whole Atmosphere Community Climate Model Version 6 (WACCM6).
965 *Journal of Geophysical Research: Atmospheres*, *124*(23), 12380–12403.
966 https://doi.org/10.1029/2019JD030943

967 Goddard, P. B., Dufour, C. O., Yin, J., Griffies, S. M., & Winton, M. (2017). CO2-Induced
968 Ocean Warming of the Antarctic Continental Shelf in an Eddying Global Climate Model.
969 *Journal of Geophysical Research: Oceans*, *122*(10), 8079–8101.
970 https://doi.org/10.1002/2017JC012849

971 Goddard, P. B., Tabor, C. R., & Jones, T. R. (2021). Utilizing Ice Core and Climate Model Data
972 to Understand Seasonal West Antarctic Variability. *Journal of Climate*, *1*(aop), 1–55.
973 https://doi.org/10.1175/JCLI-D-20-0822.1

974 Golledge, N., Keller, Elizabeth D., Gomez, N., Naughten, K. A., Bernales, J., Trusel, L. D., &
975 Edwards, T. (2019). Global environmental consequences of twenty-first-century ice-sheet
976 melt. https://doi.org/10.1038/s41586-019-0889-9

977 Gong, D., & Wang, S. (1999). Definition of Antarctic Oscillation index. *Geophysical Research*
978 *Letters*, *26*(4), 459–462. https://doi.org/10.1029/1999GL900003

979 Gorodetskaya, I. V., Tsukernik, M., Claes, K., Ralph, M. F., Neff, W. D., & Van Lipzig, N. P.
980 M. (2014). The role of atmospheric rivers in anomalous snow accumulation in East
981 Antarctica. *Geophysical Research Letters*, *41*(17), 6199–6206.
982 https://doi.org/10.1002/2014GL060881

983 Greenbaum, J. S., Blankenship, D. D., Young, D. A., Richter, T. G., Roberts, J. L., Aitken, A. R.
984 A., et al. (2015). Ocean access to a cavity beneath Totten Glacier in East Antarctica. *Nature*
985 *Geoscience 2014 8:4*, *8*(4), 294–298. https://doi.org/10.1038/ngeo2388

986 Hellmer, H. H., Kauker, F., Timmermann, R., Determann, J., & Rae, J. (2012). Twenty-first-
987 century warming of a large Antarctic ice-shelf cavity by a redirected coastal current. *Nature*
988 *2012 485:7397*, *485*(7397), 225–228. https://doi.org/10.1038/nature11064

Herraiz-Borreguero, L., & Naveira Garabato, A. C. (2022). Poleward shift of Circumpolar Deep Water threatens the East Antarctic Ice Sheet. *Nature Climate Change 2022 12:8*, *12*(8), 728–734. https://doi.org/10.1038/s41558-022-01424-3

Herraiz-Borreguero, L., Coleman, R., Allison, I., Rintoul, S. R., Craven, M., & Williams, G. D. (2015). Circulation of modified Circumpolar Deep Water and basal melt beneath the Amery Ice Shelf, East Antarctica. *Journal of Geophysical Research: Oceans*, *120*(4), 3098–3112. https://doi.org/10.1002/2015JC010697

Hosking, J. S., Orr, A., Marshall, G. J., Turner, J., & Phillips, T. (2013). The Influence of the Amundsen–Bellingshausen Seas Low on the Climate of West Antarctica and Its Representation in Coupled Climate Model Simulations. *Journal of Climate*, *26*(17), 6633–6648. https://doi.org/10.1175/JCLI-D-12-00813.1

Hosking, J. S., Orr, A., Bracegirdle, T. J., & Turner, J. (2016). Future circulation changes off West Antarctica: Sensitivity of the Amundsen Sea Low to projected anthropogenic forcing. *Geophysical Research Letters*, *43*(1), 367–376. https://doi.org/10.1002/2015GL067143

Iizuka, M., Seki, O., Wilson, D. J., Suganuma, Y., Horikawa, K., van de Flierdt, T., et al. (2023). Multiple episodes of ice loss from the Wilkes Subglacial Basin during the Last Interglacial. *Nature Communications 2023 14:1*, *14*(1), 1–10. https://doi.org/10.1038/s41467-023-37325-y

Jacobs, S. S. (1991). On the nature and significance of the Antarctic Slope Front. *Marine Chemistry*, *35*(1–4), 9–24. https://doi.org/10.1016/S0304-4203(09)90005-6

Jacobs, S. S., Hellmer, H. H., & Jenkins, A. (1996). Antarctic ice sheet melting in the Southeast Pacific, *23*(9).

Jenkins, A., & Jacobs, S. (2008). Circulation and melting beneath George VI Ice Shelf, Antarctica. *Journal of Geophysical Research: Oceans*, *113*(C4), 4013. https://doi.org/10.1029/2007JC004449

Jenkins, A., Dutrieux, P., Jacobs, S., Steig, E. J., Gudmundsson, G. H., Smith, J., & Heywood, K. J. (2016). Decadal ocean forcing and Antarctic ice sheet response: Lessons from the Amundsen Sea. *Oceanography*, *29*(4), 106–117.

https://doi.org/10.5670/OCEANOG.2016.103

Johnson, A., Hock, R., & Fahnestock, M. (2022). Spatial variability and regional trends of Antarctic ice shelf surface melt duration over 1979–2020 derived from passive microwave data. *Journal of Glaciology*, *68*(269), 533–546. https://doi.org/10.1017/JOG.2021.112

Kidson, J. W. (1988). Interannual Variations in the Southern Hemisphere Circulation. *Journal of Climate*, *1*(12), 1177–1198. Retrieved from https://doi.org/10.1175/

Kravitz, B., MacMartin, D. G., Wang, H., & Rasch, P. J. (2016). Geoengineering as a design problem. *Earth System Dynamics*, *7*(2), 469–497. https://doi.org/10.5194/esd-7-469-2016

Kravitz, B., Macmartin, D. G., Mills, M. J., Richter, J. H., Tilmes, S., Lamarque, J. F., et al. (2017). First Simulations of Designing Stratospheric Sulfate Aerosol Geoengineering to Meet Multiple Simultaneous Climate Objectives. *Journal of Geophysical Research: Atmospheres*, *122*(23), 12,616-12,634. https://doi.org/10.1002/2017JD026874

Lawrence, D. M., Fisher, R. A., Koven, C. D., Oleson, K. W., Swenson, S. C., Bonan, G., et al. (2019). The Community Land Model Version 5: Description of New Features, Benchmarking, and Impact of Forcing Uncertainty. *Journal of Advances in Modeling Earth Systems*, *11*(12), 4245–4287. https://doi.org/10.1029/2018MS001583

Lee, W. R., MacMartin, D. G., Visioni, D., Kravitz, B., Chen, Y., Moore, J. C., et al. (2023). High-Latitude Stratospheric Aerosol Injection to Preserve the Arctic. *Earth's Future*, *11*(1), e2022EF003052. https://doi.org/10.1029/2022EF003052

Liu, X., Ma, P. L., Wang, H., Tilmes, S., Singh, B., Easter, R. C., et al. (2016). Description and evaluation of a new four-mode version of the Modal Aerosol Module (MAM4) within version 5.3 of the Community Atmosphere Model. *Geoscientific Model Development*, *9*(2), 505–522. https://doi.org/10.5194/GMD-9-505-2016

Maclennan, M. L., & Lenaerts, J. T. M. (2021). Large-Scale Atmospheric Drivers of Snowfall Over Thwaites Glacier, Antarctica. *Geophysical Research Letters*, *48*(17), e2021GL093644. https://doi.org/10.1029/2021GL093644

Maclennan, M. L., Lenaerts, J. T. M., Shields, C., & Wille, J. D. (2022). Contribution of Atmospheric Rivers to Antarctic Precipitation. *Geophysical Research Letters*, *49*(18),

1045 e2022GL100585. https://doi.org/10.1029/2022GL100585

1046 MacMartin, D. G., Visioni, D., Kravitz, B., Richter, J. H., Felgenhauer, T., Lee, W. R., et al.
1047 (2022). Scenarios for modeling solar radiation modification. *Proceedings of the National*
1048 *Academy of Sciences*, *119*(33), e2202230119. https://doi.org/10.1073/PNAS.2202230119

1049 Marshall, G. J. (2003). Trends in the Southern Annular Mode from observations and reanalyses.
1050 *Journal of Climate*, *16*(24), 4134–4143. https://doi.org/10.1175/1520-
1051 0442(2003)016<4134:TITSAM>2.0.CO;2

1052 McCusker, K. E., Battisti, D. S., & Bitz, C. M. (2015). Inability of stratospheric sulfate aerosol
1053 injections to preserve the West Antarctic Ice Sheet. *Geophysical Research Letters*, *42*(12),
1054 4989–4997. https://doi.org/10.1002/2015GL064314

1055 McKay, D. I. A., Staal, A., Abrams, J. F., Winkelmann, R., Sakschewski, B., Loriani, S., et al.
1056 (2022). Exceeding 1.5°C global warming could trigger multiple climate tipping points.
1057 *Science*, *377*(6611).
1058 https://doi.org/10.1126/SCIENCE.ABN7950/SUPPL_FILE/SCIENCE.ABN7950_DATA_
1059 S1.ZIP

1060 Meinshausen, M., Nicholls, Z. R. J., Lewis, J., Gidden, M. J., Vogel, E., Freund, M., et al.
1061 (2020). The shared socio-economic pathway (SSP) greenhouse gas concentrations and their
1062 extensions to 2500. *Geoscientific Model Development*, *13*(8), 3571–3605.
1063 https://doi.org/10.5194/GMD-13-3571-2020

1064 Mo, K. C., & Higgins, R. W. (1998). The Pacific-South American modes and tropical convection
1065 during the Southern Hemisphere winter. *Monthly Weather Review*, *126*(6), 1581–1596.
1066 https://doi.org/10.1175/1520-0493(1998)126<1581:TPSAMA>2.0.CO;2

1067 Moore, J. C., Rinke, A., Yu, X., Ji, D., Cui, X., Li, Y., et al. (2014). Arctic sea ice and
1068 atmospheric circulation under the GeoMIP G1 scenario. *Journal of Geophysical Research:*
1069 *Atmospheres*, *119*(2), 567–583. https://doi.org/10.1002/2013JD021060

1070 Moorman, R., Morrison, A. K., & Hogg, A. M. C. (2020). Thermal Responses to Antarctic Ice
1071 Shelf Melt in an Eddy-Rich Global Ocean–Sea Ice Model. *Journal of Climate*, *33*(15),
1072 6599–6620. https://doi.org/10.1175/JCLI-D-19-0846.1

O'Brien, T. A., Wehner, M. F., Payne, A. E., Shields, C. A., Rutz, J. J., Leung, L. R., et al. (2022). Increases in Future AR Count and Size: Overview of the ARTMIP Tier 2 CMIP5/6 Experiment. *Journal of Geophysical Research: Atmospheres*, *127*(6), e2021JD036013. https://doi.org/10.1029/2021JD036013

Palóczy, A., Gille, S. T., & McClean, J. L. (2018). Oceanic Heat Delivery to the Antarctic Continental Shelf: Large-Scale, Low-Frequency Variability. *Journal of Geophysical Research: Oceans*, *123*(11), 7678–7701. https://doi.org/10.1029/2018JC014345

Payne, A. E., Demory, M. E., Leung, L. R., Ramos, A. M., Shields, C. A., Rutz, J. J., et al. (2020). Responses and impacts of atmospheric rivers to climate change. *Nature Reviews Earth & Environment 2020 1:3*, *1*(3), 143–157. https://doi.org/10.1038/s43017-020-0030-5

Payne, A. J., Nowicki, S., Abe-Ouchi, A., Agosta, C., Alexander, P., Albrecht, T., et al. (2021). Future Sea Level Change Under Coupled Model Intercomparison Project Phase 5 and Phase 6 Scenarios From the Greenland and Antarctic Ice Sheets. *Geophysical Research Letters*, *48*(16), e2020GL091741. https://doi.org/10.1029/2020GL091741

Perlwitz, J. (2011). Tug of war on the jet stream. *Nature Climate Change 2011 1:1*, *1*(1), 29–31. https://doi.org/10.1038/nclimate1065

Raphael, M. N., Marshall, G. J., Turner, J., Fogt, R. L., Schneider, D., Dixon, D. A., et al. (2016). The Amundsen sea low: Variability, change, and impact on Antarctic climate. *Bulletin of the American Meteorological Society*, *97*(1), 111–121. https://doi.org/10.1175/BAMS-D-14-00018.1

Ribeiro, N., Herraiz-Borreguero, L., Rintoul, S. R., McMahon, C. R., Hindell, M., Harcourt, R., & Williams, G. (2021). Warm Modified Circumpolar Deep Water Intrusions Drive Ice Shelf Melt and Inhibit Dense Shelf Water Formation in Vincennes Bay, East Antarctica. *Journal of Geophysical Research: Oceans*, *126*(8), e2020JC016998. https://doi.org/10.1029/2020JC016998

Rignot, E., & Jacobs, S. S. (2002). Rapid bottom melting widespread near antarctic ice sheet grounding lines. *Science*, *296*(5575), 2020–2023. https://doi.org/10.1126/science.1070942

Rignot, E., Mouginot, J., Scheuchl, B., Van Den Broeke, M., Van Wessem, M. J., & Morlighem,

M. (2019). Four decades of Antarctic ice sheet mass balance from 1979–2017. *Proceedings of the National Academy of Sciences of the United States of America*, *116*(4), 1095–1103. https://doi.org/10.1073/PNAS.1812883116/SUPPL_FILE/PNAS.1812883116.SD01.XLSX

Ryan, S., Hellmer, H. H., Janout, M., Darelius, E., Vignes, L., & Schröder, M. (2020). Exceptionally Warm and Prolonged Flow of Warm Deep Water Toward the Filchner-Ronne Ice Shelf in 2017. *Geophysical Research Letters*, *47*(13), e2020GL088119. https://doi.org/10.1029/2020GL088119

Scambos, T., Fricker, H. A., Liu, C. C., Bohlander, J., Fastook, J., Sargent, A., et al. (2009). Ice shelf disintegration by plate bending and hydro-fracture: Satellite observations and model results of the 2008 Wilkins ice shelf break-ups. *Earth and Planetary Science Letters*, *280*(1–4), 51–60. https://doi.org/10.1016/J.EPSL.2008.12.027

Scambos, T. A., Bohlander, J. A., Shuman, C. A., & Skvarca, P. (2004). Glacier acceleration and thinning after ice shelf collapse in the Larsen B embayment, Antarctica. *Geophysical Research Letters*, *31*(18), 18402. https://doi.org/10.1029/2004GL020670

Schlosser, E., Manning, K. W., Powers, J. G., Duda, M. G., Birnbaum, G., & Fujita, K. (2010). Characteristics of high-precipitation events in Dronning Maud Land, Antarctica. *Journal of Geophysical Research: Atmospheres*, *115*(D14), 14107. https://doi.org/10.1029/2009JD013410

Schneider, D. P., Okumura, Y., & Deser, C. (2012). Observed Antarctic interannual climate variability and tropical linkages. *Journal of Climate*, *25*(12), 4048–4066. https://doi.org/10.1175/JCLI-D-11-00273.1

Schoof, C. (2007). Ice sheet grounding line dynamics: Steady states, stability, and hysteresis. *Journal of Geophysical Research: Earth Surface*, *112*(F3). https://doi.org/10.1029/2006JF000664

Scott, R. C., Nicolas, J. P., Bromwich, D. H., Norris, J. R., & Lubin, D. (2019). Meteorological Drivers and Large-Scale Climate Forcing of West Antarctic Surface Melt. *Journal of Climate*, *32*(3), 665–684. https://doi.org/10.1175/JCLI-D-18-0233.1

Siahaan, A., Smith, R. S., Holland, P. R., Jenkins, A., Gregory, J. M., Lee, V., et al. (2022). The

1129 Antarctic contribution to 21st-century sea-level rise predicted by the UK Earth System
1130 Model with an interactive ice sheet. *Cryosphere*, *16*(10), 4053–4086.
1131 https://doi.org/10.5194/TC-16-4053-2022

1132 Smith, R., P. Jones, B. Briegleb, F. Bryan, G. Danabasoglu, J. Dennis, J. Dukowicz, C. Eden, B.
1133 Fox-Kemper, P. Gent, M. Hecht, S. Jayne, M. Jochum, W. Large, K. Lindsay, M. Maltrud,
1134 N. Norton, S. Peacock, M. Vertenstein, & S. Yeager (2010). The Parallel Ocean Program
1135 (POP) reference manual, Ocean component of the Community Climate System Model
1136 (CCSM), LANL Tech. Report, LAUR-10-01853, *141 pp*

1137 Smith, B., Fricker, H. A., Gardner, A. S., Medley, B., Nilsson, J., Paolo Nicholas Holschuh, F.
1138 S., et al. (2020). Pervasive ice sheet mass loss reflects competing ocean and atmosphere
1139 processes. *Science*, *368*(6496), 1239–1242.
1140 https://doi.org/10.1126/SCIENCE.AAZ5845/SUPPL_FILE/AAZ5845-SMITH-SM.PDF

1141 Sparrow, M., P. Chapman, & Gould, J. (Eds.) (2011). 2005 The World Ocean Circulation
1142 Experiment (WOCE) hydrographic atlas series (4 volumes). Southampton, UK:
1143 International WOCE Project Office.

1144 Spence, P., Griffies, S. M., England, M. H., Hogg, A. M. C., Saenko, O. A., & Jourdain, N. C.
1145 (2014). Rapid subsurface warming and circulation changes of Antarctic coastal waters by
1146 poleward shifting winds. *Geophysical Research Letters*, *41*(13), 4601–4610.
1147 https://doi.org/10.1002/2014GL060613

1148 Steig, E. J., Ding, Q., Battisti, D. S., & Jenkins, A. (2012). Tropical forcing of circumpolar deep
1149 water inflow and outlet glacier thinning in the amundsen sea embayment, west antarctica.
1150 *Annals of Glaciology*, *53*(60), 19–28. https://doi.org/10.3189/2012AoG60A110

1151 Stewart, A L, Thompson, A. F., Stewart, A. L., & Thompson, A. F. (2015). Eddy-mediated
1152 transport of warm Circumpolar Deep Water across the Antarctic Shelf Break. *Geophysical*
1153 *Research Letters*, *42*(2), 432–440. https://doi.org/10.1002/2014GL062281

1154 Stewart, Andrew L., Klocker, A., & Menemenlis, D. (2018). Circum-Antarctic Shoreward Heat
1155 Transport Derived From an Eddy- and Tide-Resolving Simulation. *Geophysical Research*
1156 *Letters*, *45*(2), 834–845. https://doi.org/10.1002/2017GL075677

1157 Thoma, M., Jenkins, A., Holland, D., & Jacobs, S. (2008). Modelling Circumpolar Deep Water
1158 intrusions on the Amundsen Sea continental shelf, Antarctica. *Geophysical Research*
1159 *Letters*, *35*(18). https://doi.org/10.1029/2008GL034939

1160 Thompson, A. F., Heywood, K. J., Schmidtko, S., & Stewart, A. L. (2014). Eddy transport as a
1161 key component of the Antarctic overturning circulation. *Nature Geoscience 2014 7:12*,
1162 *7*(12), 879–884. https://doi.org/10.1038/ngeo2289

1163 Thompson, D. W. J., Solomon, S., Kushner, P. J., England, M. H., Grise, K. M., & Karoly, D. J.
1164 (2011). Signatures of the Antarctic ozone hole in Southern Hemisphere surface climate
1165 change. *Nature Geoscience 2011 4:11*, *4*(11), 741–749. https://doi.org/10.1038/ngeo1296

1166 Tilmes, S. (2018). CESM1(WACCM) stratospheric aerosol Geoengineering Large Ensemble
1167 project. *Bull. Am. Meteorol. Soc.*, *99*, 2361–2371.

1168 Tilmes, Simone, Fasullo, J., Lamarque, J. F., Marsh, D. R., Mills, M., Alterskjær, K., et al.
1169 (2013). The hydrological impact of geoengineering in the Geoengineering Model
1170 Intercomparison Project (GeoMIP). *Journal of Geophysical Research: Atmospheres*,
1171 *118*(19), 11,036-11,058. https://doi.org/10.1002/JGRD.50868

1172 Tilmes, Simone, Richter, J. H., Mills, M. J., Kravitz, B., Macmartin, D. G., Vitt, F., et al. (2017).
1173 Sensitivity of Aerosol Distribution and Climate Response to Stratospheric SO2 Injection
1174 Locations. *Journal of Geophysical Research: Atmospheres*, *122*(23), 12,591-12,615.
1175 https://doi.org/10.1002/2017JD026888

1176 Trusel, L. D., Frey, K. E., Das, S. B., Karnauskas, K. B., Kuipers Munneke, P., Van Meijgaard,
1177 E., & Van Den Broeke, M. R. (2015). Divergent trajectories of Antarctic surface melt under
1178 two twenty-first-century climate scenarios. *Nature Geoscience 2015 8:12*, *8*(12), 927–932.
1179 https://doi.org/10.1038/ngeo2563

1180 Turner, J., Bracegirdle, T. J., Phillips, T., Marshall, G. J., & Scott Hosking, J. (2013). An initial
1181 assessment of antarctic sea ice extent in the CMIP5 models. *Journal of Climate*, *26*(5),
1182 1473–1484. https://doi.org/10.1175/JCLI-D-12-00068.1

1183 Turner, J., Phillips, T., Thamban, M., Rahaman, W., Marshall, G. J., Wille, J. D., et al. (2019).
1184 The Dominant Role of Extreme Precipitation Events in Antarctic Snowfall Variability.

Geophysical Research Letters, *46*(6), 3502–3511. https://doi.org/10.1029/2018GL081517

Verfaillie, D., Pelletier, C., Goosse, H., Jourdain, N. C., Bull, C. Y. S., Dalaiden, Q., et al. (2022). The circum-Antarctic ice-shelves respond to a more positive Southern Annular Mode with regionally varied melting. *Communications Earth & Environment 2022 3:1*, *3*(1), 1–12. https://doi.org/10.1038/s43247-022-00458-x

Visioni, D., MacMartin, D. G., Kravitz, B., Richter, J. H., Tilmes, S., & Mills, M. J. (2020). Seasonally Modulated Stratospheric Aerosol Geoengineering Alters the Climate Outcomes. *Geophysical Research Letters*, *47*(12), e2020GL088337. https://doi.org/10.1029/2020GL088337

Visioni, D., Kravitz, B., Robock, A., Tilmes, S., Haywood, J., Boucher, O., et al. (2023). Opinion: The scientific and community-building roles of the Geoengineering Model Intercomparison Project (GeoMIP) – past, present, and future. *Atmospheric Chemistry and Physics*, *23*(9), 5149–5176. https://doi.org/10.5194/ACP-23-5149-2023

Visioni, D., D. G. MacMartin, B. Kravitz, E. M. Bednarz, P. B. Goddard. (*submitted to Earth's Future, May 2023*). The choice of baseline period influences the assessments of the outcomes of Stratospheric Aerosol Injection.

Weertman, J. (1974). Stability of the Junction of an Ice Sheet and an Ice Shelf. *Journal of Glaciology*, *13*(67), 3–11. https://doi.org/10.3189/S0022143000023327

Whitworth, T., Orsi, A. H., Kim, S. J., Nowlin, W. D., & Locarnini, R. A. (1998). Water masses and mixing near the Antarctic Slope Front. In S. S. Jacobs & R. F. Weiss (Eds.), Ocean, ice, and atmosphere: Interactions at the Antarctic continental margins, Antarctic Research Series (Vol. 75, pp. 1–27). Washington, DC: AGU. https://doi.org/10.1029/AR075p0001

Wilks, D. S., 1997: Resampling hypothesis tests for autocorrelated fields. J. Climate, 10, 65–83, doi:10.1175/1520-0442(1997)010<0065:RHTFAF>2.0.CO;2.

Wille, J. D., Favier, V., Gorodetskaya, I. V., Agosta, C., Kittel, C., Beeman, J. C., et al. (2021). Antarctic Atmospheric River Climatology and Precipitation Impacts. *Journal of Geophysical Research: Atmospheres*, *126*(8), e2020JD033788. https://doi.org/10.1029/2020JD033788

Yeung, Y., Yiu, S., & Maycock, A. C. (2019). On the Seasonality of the El Niño Teleconnection to the Amundsen Sea Region. *Journal of Climate*, *32*(15), 4829–4845. https://doi.org/10.1175/JCLI-D-18-0813.1

Yu, L., Zhang, Z., Zhou, M., Zhong, S., Lenschow, D., Hsu, H., et al. (2012). Influence of the Antarctic Oscillation, the Pacific–South American modes and the El Niño–Southern Oscillation on the Antarctic surface temperature and pressure variations. *Antarctic Science*, *24*(1), 59–76. https://doi.org/10.1017/S095410201100054X

Zhang, Y., MacMartin, D. G., Visioni, D., Bednarz, E., and Kravitz, B. (2023). Introducing a Comprehensive Set of Stratospheric Aerosol Injection Strategies, EGUsphere [preprint], https://doi.org/10.5194/egusphere-2023-117

Zheng, F., Li, J., Clark, R. T., & Nnamchi, H. C. (2013). Simulation and Projection of the Southern Hemisphere Annular Mode in CMIP5 Models. *Journal of Climate*, *26*(24), 9860–9879. https://doi.org/10.1175/JCLI-D-13-00204.1